Physica D 435 (2022) 133257

Contents lists available at ScienceDirect

Physica D

journal homepage: www.elsevier.com/locate/physd

A potential two-scale traveling wave singularity for 3D incompressible Euler equations

Thomas Y. Hou [a], De Huang [b,*]

[a] California Institute of Technology, USA
[b] Peking University, China

ARTICLE INFO

Article history:
Received 15 October 2021
Received in revised form 21 February 2022
Accepted 10 March 2022
Available online 11 April 2022

Keywords:
Impressible Euler equations
Impressible Navier–Stokes equations
Singularity
Numerical viscosity

ABSTRACT

In this paper, we investigate a potential two-scale traveling wave singularity of the 3D incompressible axisymmetric Euler equations with smooth initial data of finite energy. The two-scale feature is characterized by the property that the center of the traveling wave approaches to the origin at a slower rate than the rate of the collapse of the singularity. The driving mechanism for this potential singularity is due to two antisymmetric vortex dipoles that generate a strong shearing layer in both the radial and axial velocity fields. Without any viscous regularization, the 3D Euler equations develop an additional small scale characterizing the thickness of the sharp front. In order to stabilize the rapidly decreasing thickness of the sharp front, we apply a vanishing first order numerical viscosity to the Euler equations. We present numerical evidence that the 3D Euler equations with this first order numerical viscosity develop a locally self-similar blowup at the origin.

1. Introduction

The question regarding the global regularity of the 3D Euler equations with smooth initial data of finite energy is one of the most challenging problems in fluid dynamics and nonlinear partial differential equations. The interested readers may consult the excellent survey [1] and the references therein. The main difficulty associated with the global regularity of the 3D Euler equations is the presence of vortex stretching, which is absent in the corresponding 2D problem. In recent years, there has been some encouraging progress in search for potential Euler singularities. In particular, Luo and Hou [2,3] presented strong numerical evidence that the 3D axisymmetric Euler equations develop a finite time singularity on the boundary. The presence of the boundary and the symmetry properties of the initial data seem to play a crucial role in generating a stable finite time singularity reported in [2,3]. In a recent paper [4], we presented strong numerical evidence that the 3D incompressible axisymmetric Navier–Stokes equations with smooth degenerate variable diffusion coefficients and smooth initial data of finite energy seem to develop a two-scale locally self-similar singularity. Unlike the Hou–Luo blowup scenario, the potential singularity for the Navier–Stokes equations with degenerate diffusion coefficients occurs at the origin.

The potential two-scale traveling wave singularity reported in [4] is induced by a potential singularity of the 3D Euler equations. Without the viscous regularization, the 3D Euler equations develop an additional small scale characterizing the thickness of the sharp front. The degenerate variable diffusion coefficients are designed in such a way that they select a stable locally self-similar two-scale solution structure but are weak enough not to suppress the potential singularity mechanism induced by the 3D Euler equations. In this paper, we will further investigate the potential two-scale traveling wave singularity of the 3D Euler equations by applying a first order numerical viscosity to the Euler equations. In some sense, we may consider the solution of the 3D Euler equations with this first order numerical viscosity as a vanishing viscosity limit of the 3D Navier–Stokes equations.

We consider the 3D Navier–Stokes equations in a periodic cylinder as in [2,3]. We impose a no-slip and no-flow boundary condition at $r = 1$ and a periodic boundary condition in the axial variable z. Let u^θ, ω^θ, and ψ^θ be the angular components of the velocity, the vorticity, and the vector stream function, respectively. By making the following change of variables [5],

$$u_1 = u^\theta/r, \quad \omega_1 = \omega^\theta/r, \quad \psi_1 = \psi^\theta/r,$$

we transform the Navier–Stokes equations into the following equivalent form

$$u_{1,t} + u^r u_{1,r} + u^z u_{1,z} = 2u_1\psi_{1,z} + \nu(t)\Delta u_1, \tag{1.1a}$$

$$\omega_{1,t} + u^r \omega_{1,r} + u^z \omega_{1,z} = 2u_1 u_{1,z} + \nu(t)\Delta\omega_1, \tag{1.1b}$$

$$-\left(\partial_r^2 + \frac{3}{r}\partial_r + \partial_z^2\right)\psi_1 = \omega_1, \tag{1.1c}$$

* Corresponding author.
E-mail addresses: hou@cms.caltech.edu (T.Y. Hou), dhuang@math.pku.edu.cn (D. Huang).

https://doi.org/10.1016/j.physd.2022.133257
0167-2789/

where $u^r = -r\psi_{1,z}$, $u^z = 2\psi_1 + r\psi_{1,r}$. We choose a time-dependent viscosity $\nu(t)$ that depends on the solution and vanishes at the potential singularity time. We use the same initial condition as that given in [4].

By choosing an appropriately designed first order numerical viscosity, we show that the potential blowup solution develops a two-scale traveling solution approaching the origin. This two-scale traveling solution shares many features similar to those reported in our previous paper [4] using degenerate variable diffusion coefficients. The two-scale traveling wave solution is characterized by the property that the center of the traveling wave, located at $(R(t), Z(t))$ with $R(t) = O((T-t)^{1/2})$, approaches to the origin at a slower rate than the rate of the collapse of the singularity, which is $Z(t) = O(T-t)$. Moreover, the odd symmetry (in z) of the initial data of ω_1 generates a dipole structure of the angular vorticity ω^θ. This antisymmetric dipole structure induces a negative radial velocity near $z = 0$, which pushes the solution near $z = 0$ towards the symmetry axis $r = 0$.

The solution generates a local hyperbolic flow in the rz-plane and leads to strong nonlinear alignment of vortex stretching. Moreover, we observe that $\psi_{1,z}(R(t), z, t)$ is a monotonically decreasing function of z and is relatively flat near $z = 0$. On the other hand, $\psi_{1,z}(R(t), z, t)$ decreases quickly beyond $z = Z(t)$ and becomes negative. Through the vortex stretching term $2\psi_{1,z}u_1$ in (1.1a), the difference in the growth rate of $\psi_{1,z}$ induces a traveling wave for u_1 that approaches $z = 0$ rapidly. The traveling wave is so strong that it overcomes the upward transport of advection. Due to the oddness of u_1 in z, the solution generates a large positive gradient u_{1z}, which contributes positively to the rapidly growth of ω_1 through the vortex stretching term $2u_1u_{1z}$ in (1.1b). The rapid growth of ω_1 in turn feeds back to the rapid growth of $\psi_{1,z}$, forming a positive feedback loop.

Another important feature is that the 2D velocity field $(u^r(t), u^z(t))$ forms a closed circle right above $(R(t), Z(t))$. The flow spins rapidly within this circle region and remains trapped inside this region. This local circle structure of the 2D velocity field is critical in stabilizing the blowup process by keeping the main parts of the u_1, ω_1 profiles inside this region and traveling towards the origin.

It is worth emphasizing that the flow dynamically develops a vacuum region between the sharp front of u_1 and the symmetry axis $r = 0$. Within the vacuum region, the angular velocity $u^\theta = ru_1$ is almost zero. Thus, there is almost no spinning around the symmetry axis and the flow effectively travels upward along the vertical direction inside the vacuum region. Outside the vacuum region, the flow spins rapidly around the symmetry axis. The local blowup solution resembles the structure of a tornado and we call the potential singularity "a tornado singularity".

The two-scale nature of the potential singular solution presents considerable challenges in obtaining a well-resolved numerical solution for the Euler equations with a first order numerical viscosity. To resolve this potential two-scale singular solution, we design an adaptive mesh by constructing two adaptive mesh maps for r and z explicitly. We use a second order finite difference method to discretize the spatial derivatives and a second order explicit Runge–Kutta method to discretize in time with an adaptive time-step size. As in [4], we need to apply a low pass filter to the velocity field to stabilize some mild instability in the tail region.

Based on the asymptotic scaling analysis that we performed in our previous paper [4], we choose the time-dependent viscosity $\nu(t)$ to vanish with the order $h(O(R(t)^2) + O(Z(t)^2))$ as $(R(t), Z(t))$ approaches the origin. This property and the scaling balance between the vortex stretching and the diffusion term imply that $R(t) = O((T-t)^{1/2})$ and $Z(t) = O(T-t)$. This further implies that the vorticity vector blows up like $O(1/(T-t)^{3/2})$ and the velocity field blows up like $O(1/(T-t)^{1/2})$. The results obtained by our scaling analysis are consistent with our numerical fitting of the blowup rates and surprisingly similar to those obtained by using the degenerate variable diffusion coefficients reported in [4]. Application of the well-known Beale–Kato–Majda blowup criteria [6] implies that the 3D Navier–Stokes equations with the time-dependent viscosity develop a finite time singularity.

We remark that the first author presented some new numerical evidence that the 3D incompressible axisymmetric Navier–Stokes equations with smooth initial data of finite energy develop nearly singular solutions at the origin [7]. The new initial condition introduced in [7] shares several attractive features of a more sophisticated initial condition constructed by Hou–Huang in [4]. This nearly singular behavior of the Navier–Stokes equations is induced by a potential finite time singularity of the 3D Euler equations reported in [8]. One important feature of the potential Euler singularity is that the solution develops nearly self-similar scaling properties that are compatible with those of the 3D Navier–Stokes equations, i.e. $Z(t) \sim (T-t)^{1/2}$. The numerical results presented in the 3D Navier–Stokes equations develop nearly singular scaling properties with maximum vorticity increased by a factor of 10^7. However, the 3D Navier–Stokes equations with this initial data do not develop a finite time singularity. On the other hand, the 3D Navier–Stokes equations with a slowly decaying time-dependent viscosity of order $O(|\log(T-t)|^{-3})$ seems to develop a finite time singularity.

There have been a number of important theoretical results for the 3D Euler equations. One of the best known results for the 3D Euler equations is the Beale–Kato–Majda non blowup criteria [1], which states that the 3D Euler equations develop a finite time singularity at time T from smooth initial data if and only if $\int_0^T \|\boldsymbol{\omega}\|_{L^\infty} dt = \infty$. In [9], Constantin–Fefferman–Majda showed that the local geometric regularity of the vorticity vector near the region of maximum vorticity could lead to the dynamic depletion of vortex stretching, thus preventing a potential finite time singularity (see also [10]). An exciting recent development is the work by Elgindi [11] (see also [12]) who proved that the 3D axisymmetric Euler equations develop a finite time singularity for a class of $C^{1,\alpha}$ initial velocity with no swirl. There have been a number of very interesting results inspired by the Hou–Lou blowup scenario [2,3], see e.g. [13–17] and the excellent survey article [18]. There has been a number of previous attempts to search for potential Euler singularities numerically. These include [19,19–26]. We refer to a recent review article [27] for a more comprehensive list of other numerical results related to potential Euler singularities.

The rest of the paper is organized as follows. In Section 2, we review some major findings of the Navier–Stokes equations using degenerate variable diffusion coefficients reported in our previous paper [4], including the first sign of singularity and the main features of the potentially singular solution. In Section 3, we investigate the 3D Navier–Stokes equations using a time-dependent vanishing viscosity. Some concluding remarks are made in Section 4.

2. The Navier–Stokes equations with degenerate variable diffusion coefficients

In this section, we review some major findings in our previous paper in which we investigated the potential two-scale traveling wave singularity for the 3D incompressible Navier–Stokes equations with degenerate variable diffusion coefficients. These results are closely related to the results that we are going to present for the 3D incompressible Euler equations with time-dependent vanishing numerical viscosity.

2.1. Description of the problem

We consider the 3D incompressible axisymmetric Navier–Stokes equations with variable diffusion coefficients:

$$\begin{aligned} \boldsymbol{u}_t + \boldsymbol{u}\cdot\nabla\boldsymbol{u} &= -\nabla p + \nabla\cdot(\nu\nabla\boldsymbol{u}) \\ \nabla\cdot\boldsymbol{u} &= 0, \end{aligned} \tag{2.1}$$

where $\boldsymbol{u} = (u^x, u^y, u^z)^T : \mathbb{R}^3 \mapsto \mathbb{R}^3$ is the 3D velocity vector, $p : \mathbb{R}^3 \mapsto \mathbb{R}$ is the scalar pressure, $\nabla = (\partial_x, \partial_y, \partial_z)^T$ is the gradient operator in $\mathbb{R}^3$, and $\nu : \mathbb{R}^3 \mapsto \mathbb{R}^{3\times 3}$ is the variable diffusion tensor. When the diffusion is absent (i.e. $\nu = \mathbf{0}$), (2.1) reduce to the 3D Euler equations. We choose the variable diffusion tensor such that

$$\nu = \mathrm{diag}(\nu^r, \nu^r, \nu^z)$$

in the cylindrical coordinates, where $\nu^r = \nu^r(r,z)$, $\nu^z = \nu^z(r,z)$ are functions of (r,z). This is equivalent to choosing $\nu = \mathrm{diag}(\nu^x, \nu^y, \nu^z)$ with $\nu^x = \nu^y = \nu^r$ in the Euclidean coordinates $(x,y,z) = (r\cos\theta, r\sin\theta, z)$. In order for ν to be a smooth function in the primitive coordinates (x,y,z), we require that $\nu^r(r,z)$, $\nu^z(r,z)$ are even functions of r with respect to $r = 0$. Let u^θ, ω^θ and ψ^θ be the angular velocity, the angular vorticity and the angular stream function, respectively. To remove the singularity, Hou and Li [5] introduced the variables

$$u_1 = u^\theta/r, \quad \omega_1 = \omega^\theta/r, \quad \psi_1 = \psi^\theta/r$$

and transformed the axisymmetric Navier–Stokes equations into the equivalent form

$$u_{1,t} + u^r u_{1,r} + u^z u_{1,z} = 2u_1\psi_{1,z} + f_{u_1}, \tag{2.2a}$$

$$\omega_{1,t} + u^r\omega_{1,r} + u^z\omega_{1,z} = 2u_1u_{1,z} + f_{\omega_1}, \tag{2.2b}$$

$$-\left(\partial_r^2 + \frac{3}{r}\partial_r + \partial_z^2\right)\psi_1 = \omega_1, \tag{2.2c}$$

$$u^r = -r\psi_{1,z}, \quad u^z = 2\psi_1 + r\psi_{1,r}, \tag{2.2d}$$

where the diffusion terms f_{u_1}, f_{ω_1} are given by

$$f_{u_1} = \nu^r\left(u_{1,rr} + \frac{3}{r}u_{1,r}\right) + \nu^z u_{1,zz} + \frac{1}{r}\nu_r^r u_1 + \nu_r^r u_{1,r} + \nu_z^z u_{1,z}, \tag{2.3a}$$

$$\begin{aligned} f_{\omega_1} = {}& \nu^r\left(\omega_{1,rr} + \frac{3}{r}\omega_{1,r}\right) + \nu^z\omega_{1,zz} + \frac{1}{r}\nu_r^r\omega_1 + \nu_r^r\omega_{1,r} + \nu_z^z\omega_{1,z} \\ & + \frac{1}{r}\left(\nu_z^r\left(u_{rr}^r + \frac{1}{r}u_r^r - \frac{1}{r^2}u^r\right)\right. \\ & + \nu_z^z u_{zz}^r - \nu_r^r\left(u_{rr}^z + \frac{1}{r}u_r^z\right) - \left.\nu_r^z u_{zz}^z\right) \\ & + \frac{1}{r}\left(\nu_{rz}^r u_r^r + \nu_{zz}^z u_z^r - \nu_{rr}^r u_r^z - \nu_{rz}^z u_z^z\right). \end{aligned} \tag{2.3b}$$

Since u_1 and ω_1 are even function of r, f_{u_1}, f_{ω_1} are well defined as long as the solution is smooth. We will solve the transformed equations (2.2) in the cylindrical region

$$\mathcal{D} = \{(r,z) : 0 \le r \le 1\},$$

and impose a periodic boundary condition in z with period 1 and the no-slip no-flow boundary condition at $r = 1$. The no=flow boundary condition is reduced to $\psi_{1,r}(1,z,t) = 0$ and the no-slip boundary in terms of the new variables u_1, ω_1, ψ_1 is given by

$$u_1(1,z,t) = 0, \quad \omega_1(1,z,t) = -\psi_{1,rr}(1,z,t), \quad \text{for all } z. \tag{2.4}$$

The no-slip boundary condition (2.4) will be enforced numerically. The initial data of u_1, ω_1 are designed to be odd function of z with respect to $z = 0$, which is automatically preserved by Eqs. (2.2). By the periodicity and the odd symmetry of the solution, we only need to solve Eqs. (2.2) in the half-period domain

$$\mathcal{D}_1 = \{(r,z) : 0 \le r \le 1, 0 \le z \le 1/2\}.$$

2.1.1. Initial data

The initial data introduced in [4] are given by

$$\begin{aligned} u_1^0(r,z) &= m_u^{(1)}\frac{u_1^{(1)}(r,z)}{\|u_1^{(1)}\|_{L^\infty}} + m_u^{(2)}u_1^{(2)}(r,z), \\ \omega_1^0(r,z) &= m_\omega^{(1)}\frac{\omega_1^{(1)}(r,z)}{\|\omega_1^{(1)}\|_{L^\infty}} + m_\omega^{(2)}\omega_1^{(2)}(r,z), \end{aligned} \tag{2.5}$$

where

$$\begin{aligned} u_1^{(1)} &= \frac{\sin(2\pi z)}{1 + (\sin(\pi z)/a_{z1})^2 + (\sin(\pi z)/a_{z2})^4} \\ &\quad \cdot \frac{r^8(1-r^2)}{1 + (r/a_{r1})^{10} + (r/a_{r2})^{14}}, \\ u_1^{(2)} &= \sin(2\pi z)\cdot r^2(1-r^2), \\ \omega_1^{(1)} &= g(r,z)\cdot\frac{\sin(2\pi z)}{1 + (\sin(\pi z)/b_{z1})^2 + (\sin(\pi z)/b_{z2})^4} \\ &\quad \cdot \frac{r^8(1-r^2)}{1 + (r/b_{r1})^{10} + (r/b_{r2})^{14}}, \end{aligned}$$

and $\omega_1^{(2)} = \sin(2\pi z)\cdot r^2(1-r^2)$.

The parameters are chosen as follows:

$$\begin{aligned} & m_u^{(1)} = 7.6\times 10^3, \quad m_u^{(2)} = 50, \quad m_\omega^{(1)} = 8.6\times 10^7, \quad m_\omega^{(2)} = 50, \\ & a_{z1} = (1.2\times 10^{-4})\pi, \quad a_{z2} = (2.5\times 10^{-4})\pi, \\ & a_{r1} = 9\times 10^{-4}, \quad a_{r2} = 5\times 10^{-3}, \\ & b_{z1} = (1\times 10^{-4})\pi, \quad b_{z2} = (1.5\times 10^{-4})\pi, \\ & b_{r1} = 9\times 10^{-4}, \quad b_{r2} = 3\times 10^{-3}. \end{aligned}$$

The function $g(r,z)$ is defined through a smooth soft-cutoff function, and it forces the profile of ω_1^0 to have a smooth "corner" shape. If we define a soft-cutoff function

$$f_{sc}(x;a,b) = \frac{e^{(x-a)/b}}{e^{(x-a)/b} + e^{-(x-a)/b}}, \tag{2.6}$$

then $g(r,z)$ is given by the formula

$$\begin{aligned} g(r,z) = {}& \big(1 - f_{sc}(\sin(\pi z)/\pi; 0.7b_{z1}, 0.5b_{z1}) \\ & \cdot f_{sc}(r; b_{r1} + 0.5b_{z1}, b_{z1})\big) \\ & \times \big(1 - f_{sc}(-\sin(\pi z)/\pi; 0.7b_{z1}, 0.5b_{z1}) \\ & \cdot f_{sc}(r; b_{r1} + 0.5b_{z1}, b_{z1})\big). \end{aligned}$$

Zoom-in veiws of the profiles of u_1^0 and ω_1^0 are provided in Fig. 2.1. Moreover, the initial stream function ψ_1^0 is obtained from ω_1^0 via the Poisson equation

$$-\left(\partial_r^2 + \frac{3}{r}\partial_r + \partial_z^2\right)\psi_1^0(r,z) = \omega_1^0(r,z) \quad \text{for } (r,z)\in\mathcal{D}_1,$$

subject to the homogeneous boundary conditions

$$\psi_{1,r}^0(0,z) = \psi_1^0(1,z) = \psi_1^0(r,0) = \psi_1^0(r,1/2) = 0.$$

This initial condition was designed based on several principles described in [4]. These principles are critical for the solution to trigger a positive feed back mechanism that leads to a sustainable focusing blowup.

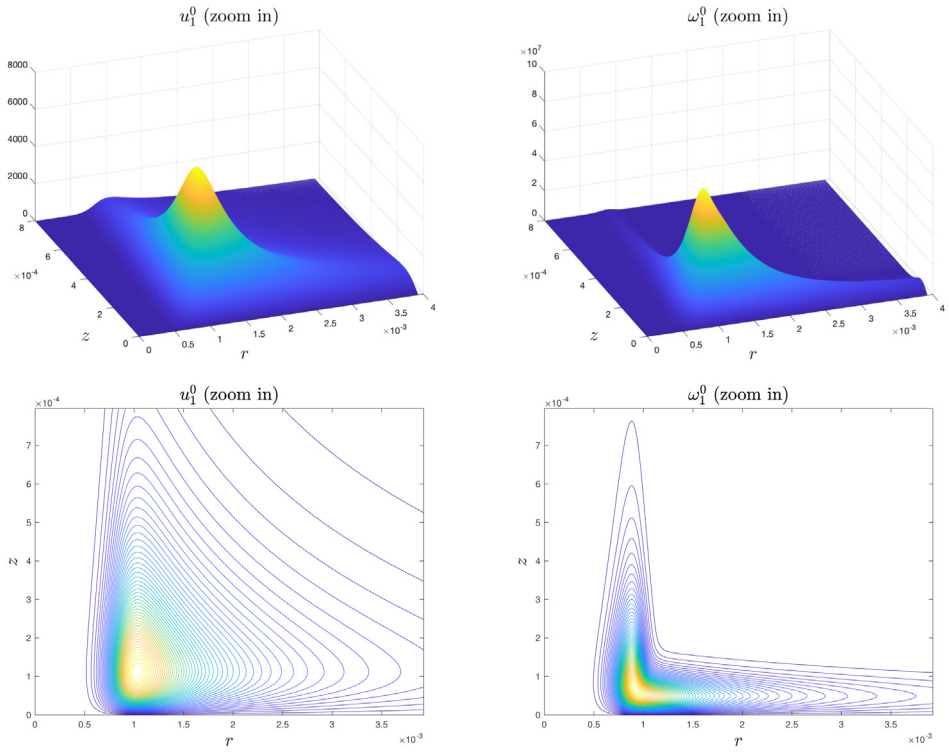

Fig. 2.1. Profiles (first row) and contours (second row) of the initial data u_1^0 and ω_1^0 on a zoom-in domain $(r, z) \in [0, 4 \times 10^{-3}] \times [0, 8 \times 10^{-4}]$.

2.1.2. Variable diffusion coefficients

We choose the variable diffusion coefficients ν^r, ν^z to be the sum of a space-dependent part and a time-dependent part:

$$\nu^r(r,z,t) = \frac{10r^2}{1+10^8 r^2} + \frac{10^2(\sin(\pi z)/\pi)^2}{1+10^{11}(\sin(\pi z)/\pi)^2} + \frac{2.5\times 10^{-2}}{\|\omega^\theta(t)\|_{L^\infty}}, \tag{2.7a}$$

$$\nu^z(r,z,t) = \frac{10^{-1}r^2}{1+10^8 r^2} + \frac{10^4(\sin(\pi z)/\pi)^2}{1+10^{11}(\sin(\pi z)/\pi)^2} + \frac{2.5\times 10^{-2}}{\|\omega^\theta(t)\|_{L^\infty}}. \tag{2.7b}$$

We remark that the space-dependent parts of ν^r, ν^z are very small (below 10^{-7}) on the whole domain and are of order $O(r^2)+O(z^2)$ for $r \le 10^{-4}$ and $z \le 10^{-5}$. The time-dependent part in ν^r, ν^z is also very small (below 4×10^{-7} initially) due to the rapid increase of $\|\omega^\theta(t)\|_{L^\infty}$ in time and is non-essential for the potential singularity formation in our scenario. In fact, removing the time-dependent part of ν^r, ν^z after the solution enters a stable phase would have no impact on the solution behavior. The degeneracy of the diffusion is crucial for the solution to develop a two-scale singularity. On the other hand, the $O(1)$ diffusion in the far field prevents the shearing induced instability from destabilizing the locally self-similar solution.

The potential blowup solution we compute develops a long thin tail structure. In [4], we applied a second order low pass filtering to control the mild oscillations induced by the shearing flow along the thin tail. The overall numerical method is still second order in space and time. We have performed careful convergence to confirm that our numerical method is indeed second order accurate, see [4] for detailed convergence study of various solution quantities.

2.2. Profile evolution

In this subsection, we investigate how the profiles of the solution evolve in time. We have computed the numerical solution up to time $t = 1.76 \times 10^{-4}$ when it is still well resolved. The computation roughly consists of three phases: a warm-up phase ($t \in [0, 1.6\times 10^{-4}]$), a stable phase ($t \in (1.6\times 10^{-4}, 1.75\times 10^{-4}]$), and a phase afterwards ($t > 1.75\times 10^{-4}$). In the warm-up phase, the solution evolves from the smooth initial data into a special structure. In the stable phase, the solution maintains a certain geometric structure and blows up stably. Beyond the stable phase, the solution exhibits some unstable features that may be due to under-resolution.

In Fig. 2.2, we illustrate the evolution of u_1, ω_1 in the late warm-up phase by showing the solution profiles at 3 different times $t = 1.38\times 10^{-4}$, 1.55×10^{-4}, 1.63×10^{-4}. The magnitudes of u_1, ω_1 grow rapidly during this time period. The support of the solution travels towards the origin. The profile of u_1 develops sharp gradients along both r and z directions. Let $(R(t), Z(t))$ denote the maximum location of $u_1(r, z, t)$. We will always us this notation throughout the paper. Fig. 2.3 shows the cross sections of u_1 going through the point $(R(t), Z(t))$ in both directions. We also observe a "vacuum" region where u_1, ω_1 are almost 0 between the sharp front and the symmetry axis $r = 0$. It is interesting to note that both u_1 and ω_1 form a long tail part propagating towards the far field. The boundary of the vacuum region plays a role similar to the moving boundary in a two-phase flow.

2.3. Two scales

One important feature of the solution is that it develops a two-scale structure. To see this, we plot the trajectory of the maximum location $(R(t), Z(t))$ of $u_1(r, z, t)$ in Fig. 2.4 (the first column). We can see that the trajectory tends to become parallel to the horizontal axis $z = 0$ in the stable phase, implying that $Z(t)$ converges to 0 much faster than $R(t)$. To confirm the two-scale solution structure, we plot in the second column of Fig. 2.4 the ratio $R(t)/Z(t)$. We observe that this ratio grows rapidly in time, especially in the stable phase. In Fig. 2.5, we show the profiles and level sets of u_1, ω_1 at time $t = 1.63 \times 10^{-4}$ in a square domain

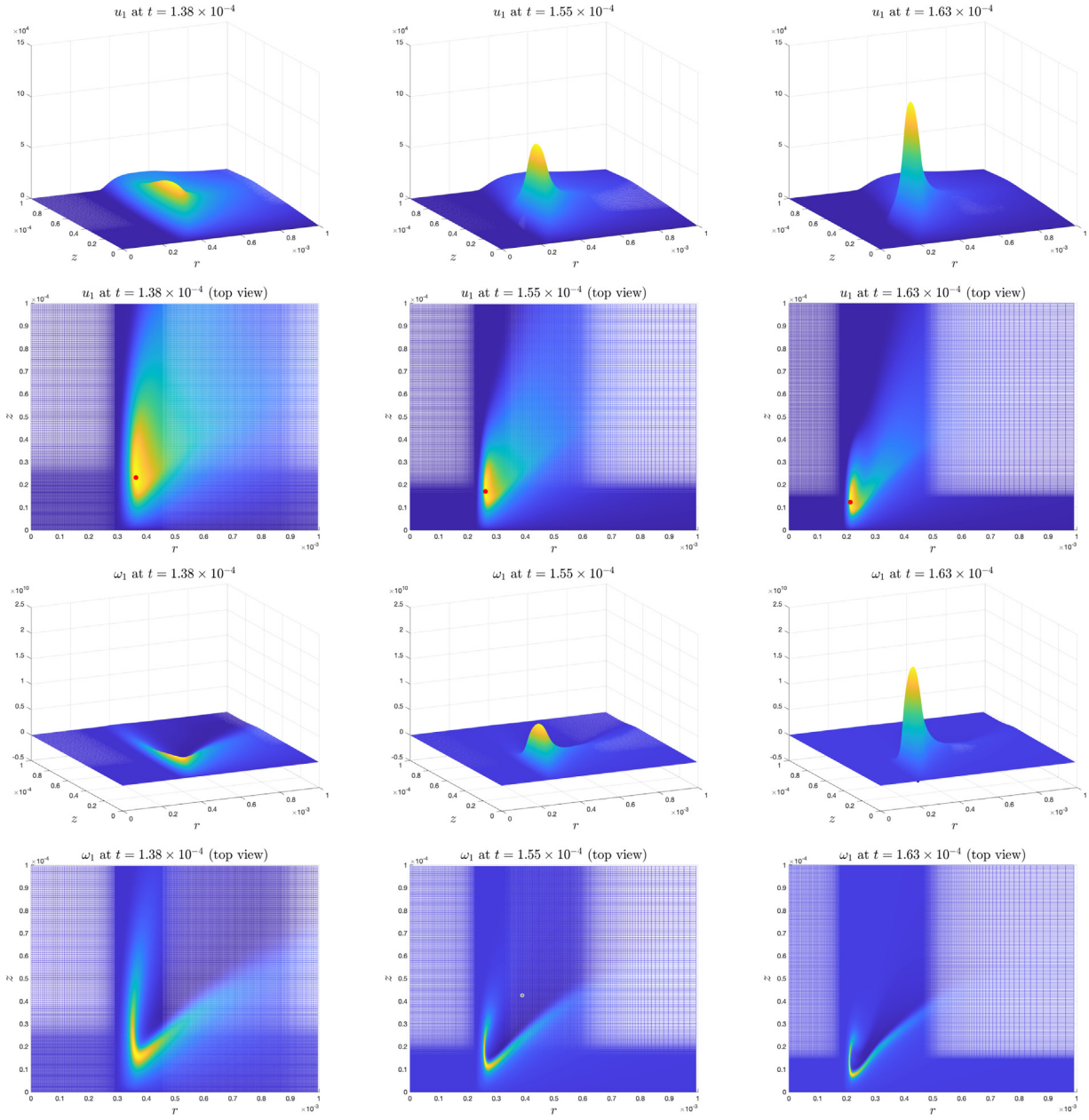

Fig. 2.2. The evolution of the profiles of u_1 (row 1 and 2) and ω_1 (row 3 and 4) in Case 1. Line 1 and 3 are the profiles of u_1, ω_1 at three different times; Line 2 and 4 are the corresponding top-views. The red dot is the location of maximum u_1.

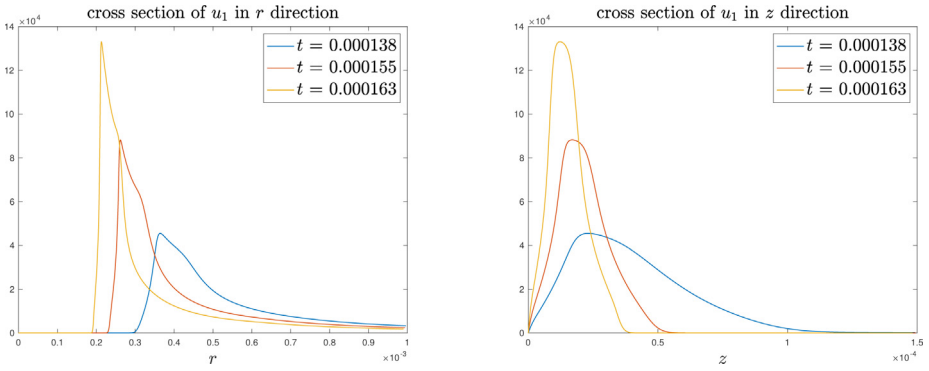

Fig. 2.3. Cross sections of u_1 in both directions at different times.

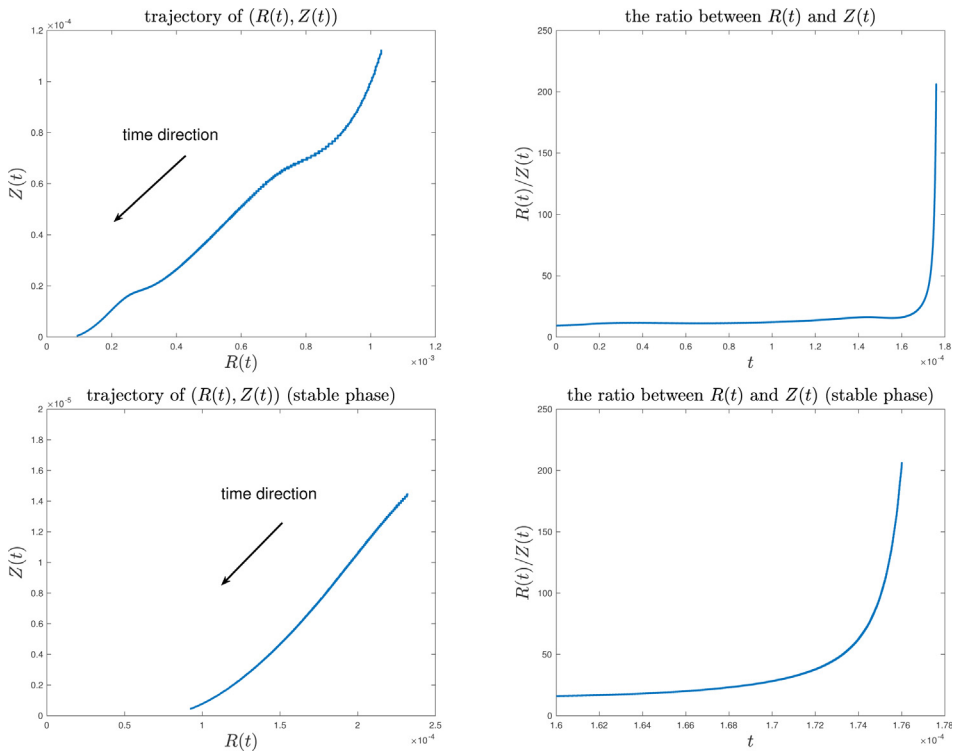

Fig. 2.4. The trajectory of $(R(t), Z(t))$ and the ratio $R(t)/Z(t)$ as a function of time for $t \in [0, 1.76 \times 10^{-4}]$. First row: the whole computation. Second row: the stable phase.

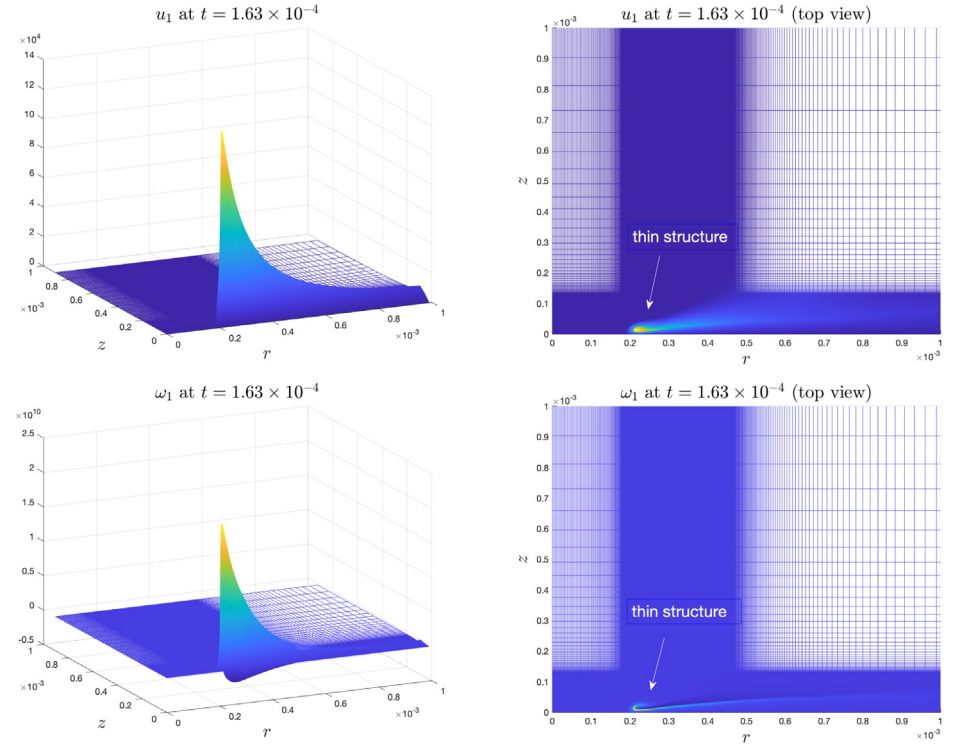

Fig. 2.5. Profiles and level sets of u_1 (first row) and ω_1 (second row) at time $t = 1.63 \times 10^{-4}$ in the square domain $\{(r, z) : 0 \le r \le 10^{-3}, 0 \le z \le 10^{-3}\}$.

$\{(r, z) : 0 \le r \le 10^{-3}, 0 \le z \le 10^{-3}\}$. The profiles are extremely thin in the z direction, reflecting the scale of $Z(t)$ (the smaller scale). On the other hand, the distance between the sharp front and the symmetry axis $r = 0$ is much longer, which corresponds to the scale of $R(t)$.

Despite the thin structure when we view the solution in a square domain, the solution has a smooth locally isotropic profile. In Fig. 2.6, we plot the local isotropic profiles of u_1, ω_1 near the sharp front at a later time $t = 1.75 \times 10^{-4}$. These profiles are very smooth with respect to the smaller scale $Z(t)$. These local

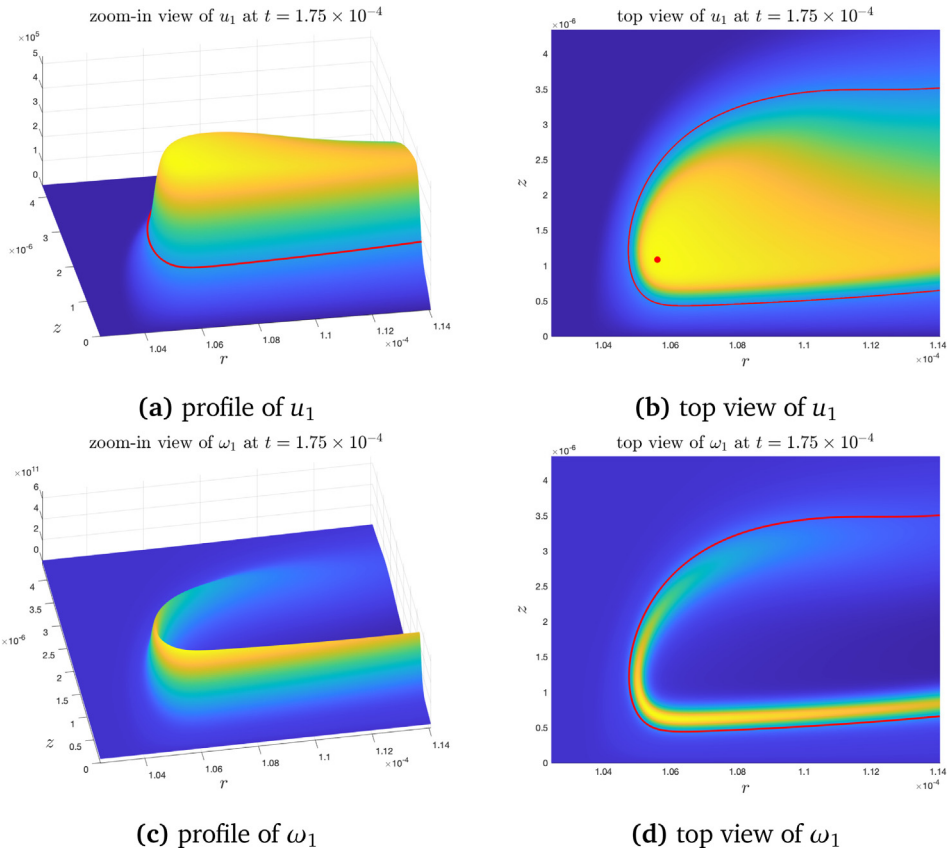

(a) profile of u_1 **(b)** top view of u_1

(c) profile of ω_1 **(d)** top view of ω_1

Fig. 2.6. Zoom-in views of u_1, ω_1 at time $t = 1.75 \times 10^{-4}$. First row: profile and tow view of u_1. Second row: profile and top view of ω_1. The red curve (in all figures above) is the level set of u_1 for the value $0.3\|u_1\|_{L^\infty}$, and the red point is the maximum location of u_1.

isotropic profiles are quite stable after the solution enters the stable phase. We will further investigate this in Section 2.9.

We can also interpret the evolution of u_1 as some form of "density", as we can see in Fig. 2.6(a) and (b) that the profile of u_1 has a clear "two-phase" feature. The sharp cliff surrounding the bulk part of u_1 behaves like a "moving boundary" between the two phases (see the red level set of u_1 in Fig. 2.6). In the interior of the "moving boundary" (where the red point is located), u_1 is large and smooth. We can interpret this as a heavier fluid phase. On the exterior of the "moving boundary", u_1 is close to 0. We can call this a vacuum phase of the fluid. The evolution of the u_1 profile thus can be locally interpreted as the evolution of a two-phase flow separated by a "moving boundary".

It is interesting to note that the contours of u_1 and ω_1 seem to have the same shape. The thin structure of ω_1 behaves like a regularized 1D delta function supported along the "moving boundary". In [4], we showed that this phenomena is a consequence of a two-scale, locally self-similar blowup.

2.4. Rapid growth

In this subsection, we report some results on the rapid growth of the solution. The maximums of $|u_1|$, $|\omega_1|$ and $|\boldsymbol{\omega}|$ as functions of time are reported in Fig. 2.7. Here

$$\boldsymbol{\omega} = (\omega^\theta, \omega^r, \omega^z)^T = (r\omega_1, -ru_{1,z}, 2u_1 + ru_{1,r})^T$$

is the vorticity vector, and

$$|\boldsymbol{\omega}| = \sqrt{(\omega^\theta)^2 + (\omega^r)^2 + (\omega^z)^2}.$$

We can see that these variables grow rapidly in time and much faster than a double-exponential rate (see the second row in Fig. 2.7). Using a standard argument, it is not hard to show that the solution to the Navier–Stokes Eqs. (2.1) with a degenerate diffusion coefficient ν ceases to exist in some regularity class H^s ($s \geq 3$) beyond a time instant T if and only if

$$\int_0^T \|\nabla \boldsymbol{u}(t)\|_{L^\infty} \, dt = +\infty.$$

Since $\|\boldsymbol{\omega}\|_{L^\infty} \lesssim \|\nabla \boldsymbol{u}\|_{L^\infty}$, the rapid growth of maximum vorticity $\|\boldsymbol{\omega}\|_{L^\infty}$ is still a good indicator for a finite time singularity in the case of a degenerate diffusion coefficient. We will demonstrate in Section 2.8 that the growth of $\|\boldsymbol{\omega}\|_{L^\infty}$ has a very nice fitting to an inverse power law

$$\|\boldsymbol{\omega}(t)\|_{L^\infty} \approx (T - t)^{-\gamma}$$

for some power $\gamma > 1$. This would imply that the solution develops a potential singularity at a finite time T.

2.5. Velocity field

In this subsection, we investigate the feature of the velocity field by looking at the induced streamlines. An induced streamline $\{\Phi(s; X_0)\}_{s \geq 0} \subset \mathbb{R}^3$ is completely determined by the background velocity $\boldsymbol{u}$ and the initial point $X_0 = (x_0, y_0, z_0)^T$ through the initial value problem

$$\frac{\partial}{\partial s}\Phi(s; X_0) = \boldsymbol{u}(\Phi(s; X_0)), \quad s \geq 0; \quad \Phi(0; X_0) = X_0.$$

We will generate different streamlines with different initial points $X_0 = (r_0 \cos(2\pi\theta), r_0 \sin(2\pi\theta), z_0)^T$. Due to the axisymmetry of the velocity field, the streamline depends on (r_0, z_0) only.

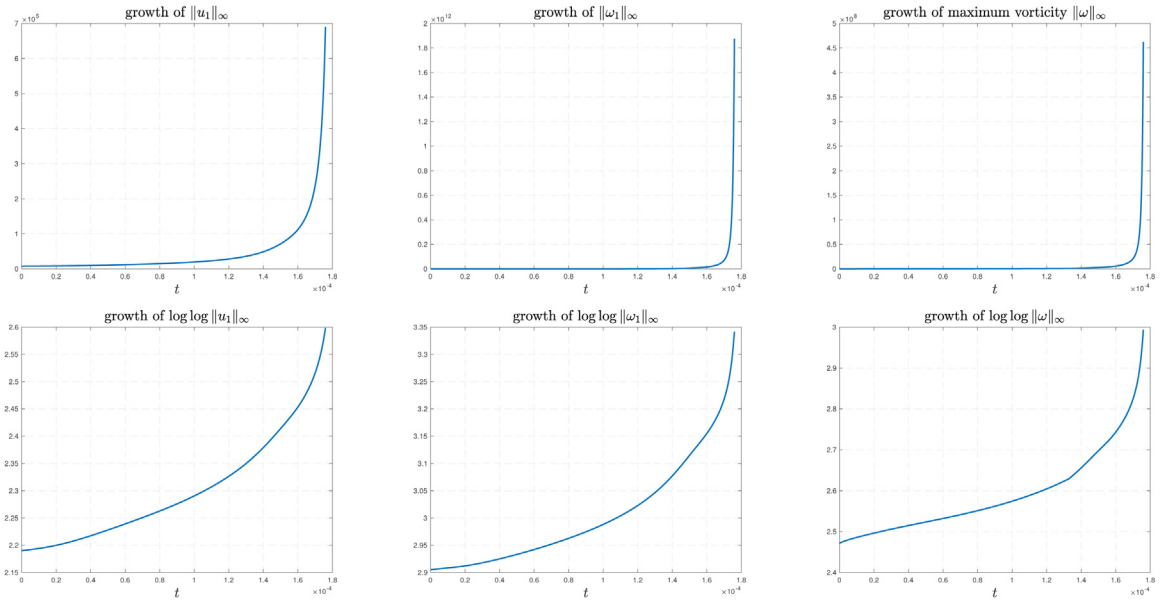

Fig. 2.7. First row: the growth of $\|u_1\|_{L^\infty}$, $\|\omega_1\|_{L^\infty}$ and $\|\boldsymbol{\omega}\|_{L^\infty}$ as functions of time. Second row: $\log\log\|u_1\|_{L^\infty}$, $\log\log\|\omega_1\|_{L^\infty}$ and $\log\log\|\boldsymbol{\omega}\|_{L^\infty}$.

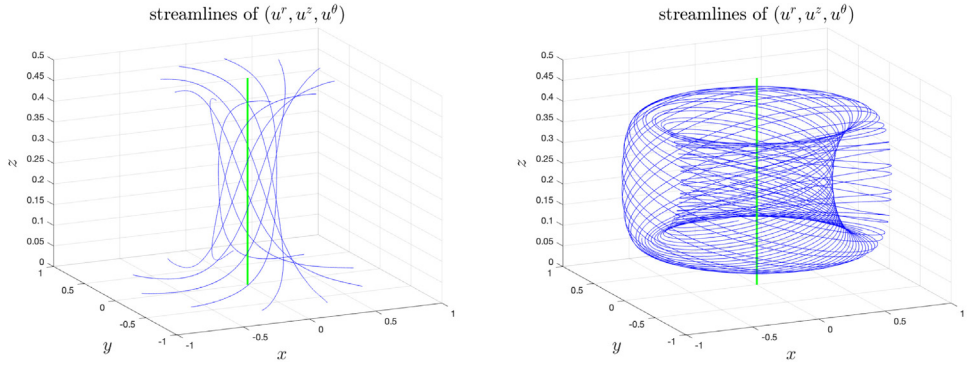

(a) $r_0 = 0.8$, $z_0 = 0.01$ **(b)** $r_0 = 0.8$, $z_0 = 0.1$

Fig. 2.8. The streamlines of $(u^r(t_0), u^\theta(t_0), u^z(t_0))$ at time $t_0 = 1.7 \times 10^{-4}$ with initial points given by (a) $(r_0, z_0) = (0.8, 0.01)$ and (b) $(r_0, z_0) = (0.8, 0.1)$. The green pole is the symmetry axis $r = 0$.

2.5.1. A tornado singularity

In Fig. 2.8, we plot the streamlines induced by the velocity field $\boldsymbol{u}(t)$ at $t_0 = 1.7 \times 10^{-4}$ in the whole cylinder domain $\mathcal{D}_1 \times [0, 2\pi]$ for different initial points with (a) $(r_0, z_0) = (0.8, 0.01)$ and (b) $(r_0, z_0) = (0.8, 0.1)$. The velocity field resembles that of a tornado spinning around the symmetry axis (the green pole). In the case when streamline starts near $z = 0$ as in Fig. 2.8(a), it will first approach the symmetry axis and then travels upward towards $z = 1/2$ while spinning around the symmetry axis. After it gets close to $z = 1/2$, it turns outward away from the symmetry axis. On the other hand, if the initial point is higher (in the z coordinate) as in Fig. 2.8(b), the streamline will travel in an "inward–upward–outward–downward" cycle in the rz-coordinates but does not get close to the symmetry axis. In the mean time, it circles around the symmetry axis.

We also examine the streamlines near the blowup region. Fig. 2.9 shows the streamlines at time $t_0 = 1.7 \times 10^{-4}$ for different initial points near the maximum location $(R(t_0), Z(t_0))$ of $u_1(t_0)$. The red ring represents the location of $(R(t_0), Z(t_0))$, and the green pole is the symmetry axis $r = 0$. The 3 settings of (r_0, z_0) are as follows.

(a) $(r_0, z_0) = (2R(t_0), 0.01Z(t_0))$. The streamline starts near $z = 0$ and below the red ring $(R(t_0), Z(t_0))$. It first travels towards the symmetry axis and then travels upward away from $z = 0$. There is almost no spinning since $u^\theta = ru_1$ is small in this region.

(b) $(r_0, z_0) = (1.05R(t_0), 2Z(t_0))$. The streamline starts right above the ring $(R(t_0), Z(t_0))$. It gets trapped in a local region and spins rapidly around the symmetry axis periodically.

(c) $(r_0, z_0) = (1.5R(t_0), 3Z(t_0))$. The streamline starts even higher and away from the ring $(R(t_0), Z(t_0))$. It spins upward and travels away from the blowup region.

2.5.2. The 2D flow

To gain better understanding for the 3D velocity field as shown in Fig. 2.9, we study the 2D velocity field (u^r, u^z) in the computational domain $\mathcal{D}_1$. In Fig. 2.10(a), we plot the vector field of $(u^r(t), u^z(t))$ at $t_0 = 1.7 \times 10^{-4}$ in a local microscopic domain $[0, R_b] \times [0, Z_b]$, where $R_b = 2.5R(t_0) \approx 3.97 \times 10^{-4}$ and $Z_b = 8Z(t_0) = 4.50 \times 10^{-5}$. Fig. 2.10(b) is a schematic for the vector field in Fig. 2.10(a).

The vector plot shows that the streamline below $(R(t_0), Z(t_0))$ first travels towards $r = 0$ and then move upward away from $z = 0$. Note that the angular velocity $u^\theta = ru^1$ is almost 0 in the region near $z = 0$. As the flow gets close to $r = 0$, the

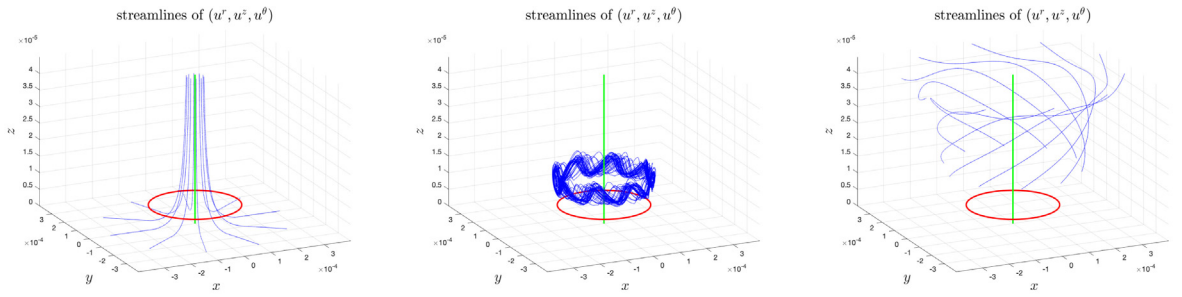

(a) $r_0 = 2R(t_0), z_0 = 0.01Z(t_0)$ **(b)** $r_0 = 1.05R(t_0), z_0 = 2Z(t_0)$ **(c)** $r_0 = 1.5R(t_0), z_0 = 3Z(t_0)$

Fig. 2.9. The streamlines of $(u^r(t_0), u^\theta(t_0), u^z(t_0))$ at time $t_0 = 1.7 \times 10^{-4}$ with initial points given by (a) $(r_0, z_0) = (2R(t_0), 0.01Z(t_0))$, (b) $(r_0, z_0) = (1.05R(t_0), 2Z(t_0))$ and (c) $(r_0, z_0) = (1.5R(t_0), 3Z(t_0))$. $(R(t_0), Z(t_0))$ is the maximum location of $u_1(t_0)$, indicated by the red ring. The green pole is the symmetry axis $r = 0$.

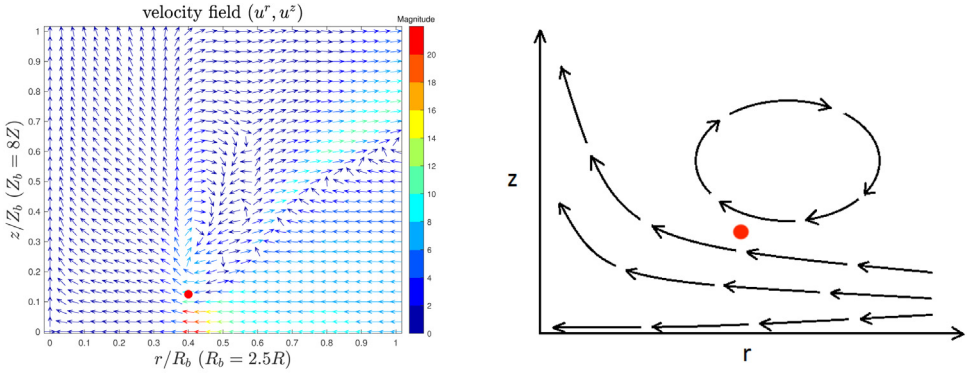

(a) the velocity field (u^r, u^z) **(b)** a schematic

Fig. 2.10. (a) The velocity field $(u^r(t_0), u^z(t_0))$ near the maximum location $(R(t_0), Z(t_0))$ of $u_1(t_0)$ (the red point) at $t_0 = 1.7 \times 10^{-4}$. The color corresponds to the magnitude of $\sqrt{(u^r)^2 + (u^z)^2}$. The size of the domain has been rescaled. (b) A schematic of the vector field near the point $(R(t_0), Z(t_0))$.

strong axial velocity u^z transports u_1 from near $z = 0$ upward along the z direction, creating a vacuum region between the sharp front of u_1 and the symmetry axis $r = 0$. Moreover, we observe that the velocity field $(u^r(t_0), u^z(t_0))$ forms a closed circle right above $(R(t_0), Z(t_0))$ as illustrated in Fig. 2.10(b) and the streamline is hence trapped in this circle region in the rz-plane. This local circle structure of the 2D velocity field plays an essential role in stabilizing the blowup process since the majority of u_1, ω_1 is retained within this region instead of being transported upward.

The velocity field $(u^r(t), u^z(t))$ also explains the sharp local structures of u_1, ω_1 shown in Fig. 2.6(a),(b). Fig. 2.11 shows the level sets of u^r, u^z at $t_0 = 1.7 \times 10^{-4}$. The radial velocity u^r has a strong shearing layer below $(R(t_0), Z(t_0))$ (the red point). This shearing contributes to the sharp gradient of u_1 in the z direction. Similarly, the axial velocity u^z also has a strong shearing layer close to the point $(R(t_0), Z(t_0))$, which explains the sharp front of u_1 in the r direction.

2.6. Understanding the blowup mechanism

In this subsection, we would like to further examine several critical factors that lead to a sustainable blowup solution.

2.6.1. Vortex dipoles and hyperbolic flow

First of all, we note that the 2D velocity field (u^r, u^θ) can be extended to the negative r plane as an even function of r. The odd symmetry (in z) of ω_1 constitutes a dipole structure of the angular vorticity ω^θ, which induces a hyperbolic flow in the rz-plane and a pair of antisymmetric (with respect to z) local circulations. This pair of antisymmetric convective circulations has the desirable property of pushing the solution near $z = 0$ towards $r = 0$. In Fig. 2.12, we show the dipole structure of the initial data ω_1^0 in a local symmetric region $(r, z) \in [0, 3 \times 10^{-3}] \times [-3 \times 10^{-4}, 3 \times 10^{-4}]$ and the hyperbolic velocity field induced by it. One of the important features of the antisymmetric vortex dipoles is that it generates a negative radial velocity near $z = 0$, which pushes the solution towards $r = 0$.

2.6.2. The odd symmetry and sharp gradient of u_1

First of all, we observe that the driving force for the growth of ω_1 comes from the vortex stretching term $2(u_1^2)_z$. Due to the odd symmetry of u_1, $(u_1^2)_z$ is positive and large somewhere between $z = Z(t)$ and $z = 0$, which leads to the rapid growth of ω_1 near $z = 0$. A strong dipole structure of the angular vorticity ω^θ induces a strong negative radial velocity u^r in between the dipole (see Fig. 2.12). From the relationship $\psi_{1,z} = -u^r/r$, the growth of $-u^r$ around $z = 0$ implies the growth of $\psi_{1,z}$, which in turn contributes to the rapid growth of u_1 through the vortex stretching term $2\psi_{1,z}u_1$ in the u_1 Eq. (2.2a).

Using the oddness of ψ_1 as a function of z and the Poisson Eq. (2.2c), one can show that $\psi_{1,z}$, as a function of z, achieves its local maximum at $z = 0$ in a neighborhood of $z = 0$ in the singular region. Moreover, $\psi_{1,z}$ decreases rapidly beyond $z = Z(t)$ and even becomes negative further away from $Z(t)$. The difference in the growth rate of $\psi_{1,z}$ as a function of z and the nonlinear vortex stretching term $2\psi_{1,z}u_1$ in the u_1 equation induce a traveling wave for u_1 propagating towards $z = 0$. The traveling wave is so strong that it overcomes the upward transport of advection along the z direction. The fact that the maximum location of u_1 traveling towards $z = 0$ generates an even sharper gradient of u_1^2 in the z direction. The whole coupling

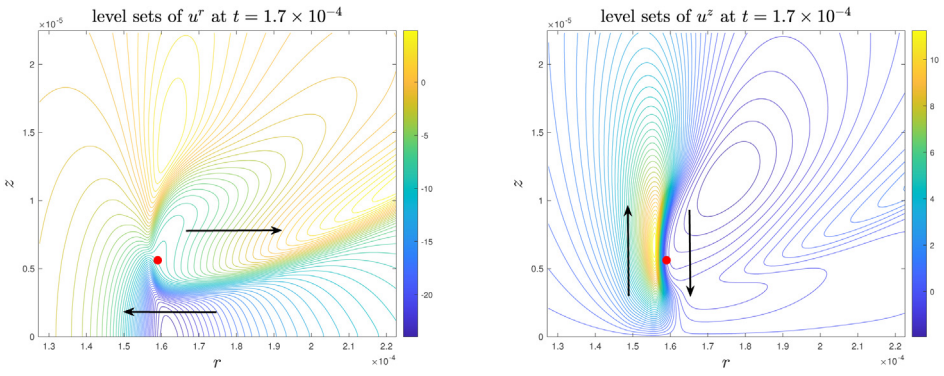

Fig. 2.11. The level sets of u^r (left) and u^z (right) at $t_0 = 1.7 \times 10^{-4}$. The red point is the maximum location $(R(t_0), Z(t_0))$ of $u_1(t_0)$.

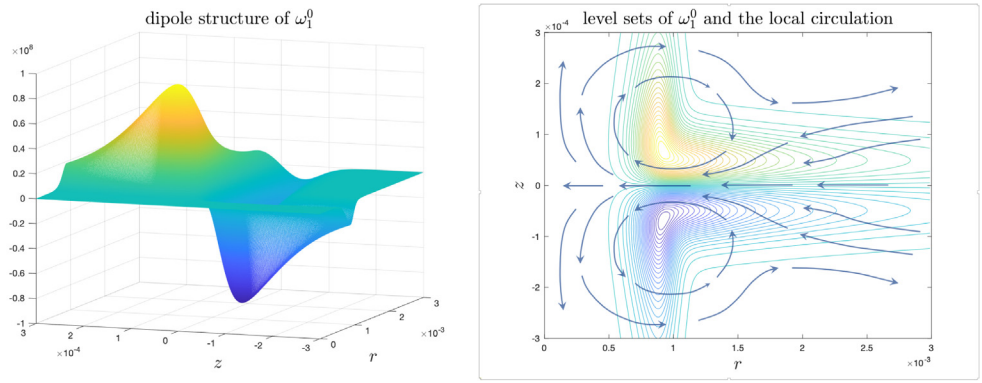

Fig. 2.12. The dipole structure of the initial data ω_1^0 and the induced local velocity field.

mechanism described above forms a positive feedback loop,

$$(u_1^2)_z \uparrow \implies \omega_1 \uparrow \implies \psi_{1,z} \uparrow \implies u_1 \uparrow \implies (u_1^2)_z \uparrow . \tag{2.8}$$

To trigger this mechanism, it is important that the maximum location of ω_1 should align with the location where $u_{1,z}$ is positive and large, which is slightly lower (in z) than the maximum location of u_1. This is one of the guiding principles in the construction of our initial data.

Fig. 2.13 demonstrates the alignment between $\psi_{1,z}$ and u_1. From Fig. 2.13(b), we can see that $\psi_{1,z}(R(t), z, t)$ is monotonically decreasing for $z \in [0, 2Z(t)]$ and relatively flat for $z \in [0, 0.5Z(t)]$, and is comparable to u_1 in magnitude. This strong quadratic alignment between u_1 and ψ_{1z} leads to the rapid growth of u_1 and pushes $Z(t)$ moving towards $z = 0$. In Fig. 2.13(c), we plot the alignment ratio $\psi_{1,z}(R(t), Z(t), t)/u_1(R(t), Z(t), t)$. One can see that the ratio $\psi_{1,z}/u_1$ settles down to a stable value in the stable phase which is characterized by the time interval $[1.6 \times 10^{-4}, 1.75 \times 10^{-4}]$. Within this stable phase, we have $\psi_{1,z}(R(t), Z(t), t) \sim u_1(R(t), Z(t), t)$. The formally quadratic alignment between u_1 and ψ_{1z} at the maximum location of u_1 implies that maximum u_1 should blow up like $(T - t)^{-1}$ for some finite time T.

2.7. The pressure

In this subsection, we study the pressure p, which may explain the formation of the potential two-scale blowup from a more physical perspective. Formally, the pressure is related to the velocity field through the Eqs. (2.1), where the variable diffusion coefficient ν now affects the value of p. In order to only investigate the physical meaning of the pressure distribution, we choose to compute the p as the pressure characterized by the original 3D Navier–Stokes equations:

$$-\Delta p = \mathrm{tr}[(\nabla \boldsymbol{u})^2].$$

This relation only defines p up to a function of t. A general way to normalize p for the Navier–Stokes equations in the whole space $\mathbb{R}^3$ is by assuming $p = 0$ at infinity. Accordingly, we will normalize p in our computation by setting $p = 0$ at $(r, z) = (1, 0)$, since the outer boundary $r = 1$ can be viewed as the far field when compared with the vanishing blowup scale.

In Fig. 2.14, we plot the profile of the pressure p in a domain $[8 \times 10^{-4}, 8 \times 10^{-5}]$ at $t = 1.7 \times 10^{-4}$ and compare it with the profile of u_1. We can see that the pressure develops a deep well that coincides with the peak of u_1, and the maximum location of u_1 (the red point) falls right at the bottom of the pressure well. The pressure drop around $(R(t), Z(t))$ forms an attractive hole that prevents the "mass" of u_1 from escaping the traveling front of the solution. More rigorously, the fluid particles with high angular velocity are trapped within the low pressure region and forced to travel towards $(r, z) = (0, 0)$. This explains the "two-phase" feature of u_1 and the "vacuum" region to the left hand side of the blowup region.

The low pressure well also explains the closed circle in the 2D velocity field (u^r, u^z) as shown in Fig. 2.10. Due to the attracting effect of the pressure well, the flow field is forced to circle around locally near the maximum location of u_1. Moreover, we can see that the pressure has large gradient in the r direction as the maximum of p is actually achieved just to the left of the pressure well. The sharp gradient of p here forms a strong force pointing in the opposite direction of the traveling wave and thus generates a sharp front in the solution. This provides another explanation for the formation of the sharp front in u_1 from the physical perspective.

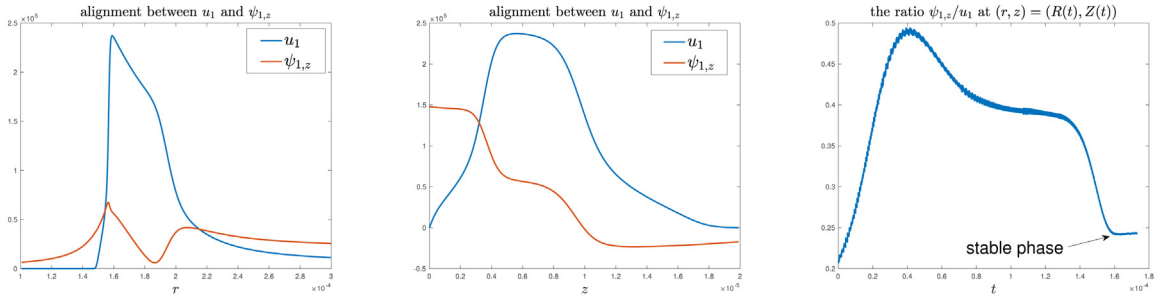

(a) r cross sections of u_1, $\psi_{1,z}$ **(b)** z cross sections of u_1, $\psi_{1,z}$ **(c)** $\psi_{1,z}/u_1$ as a function of time

Fig. 2.13. The alignment between u_1 and $\psi_{1,z}$. (a) and (b): cross sections of u_1 and $\psi_{1,z}$ through the point $(R(t), Z(t))$ at $t = 1.7 \times 10^{-4}$. (c): the ratio $\psi_{1,z}/u_1$ at the point $(R(t), Z(t))$ as a function of time up to $t = 1.75 \times 10^{-4}$.

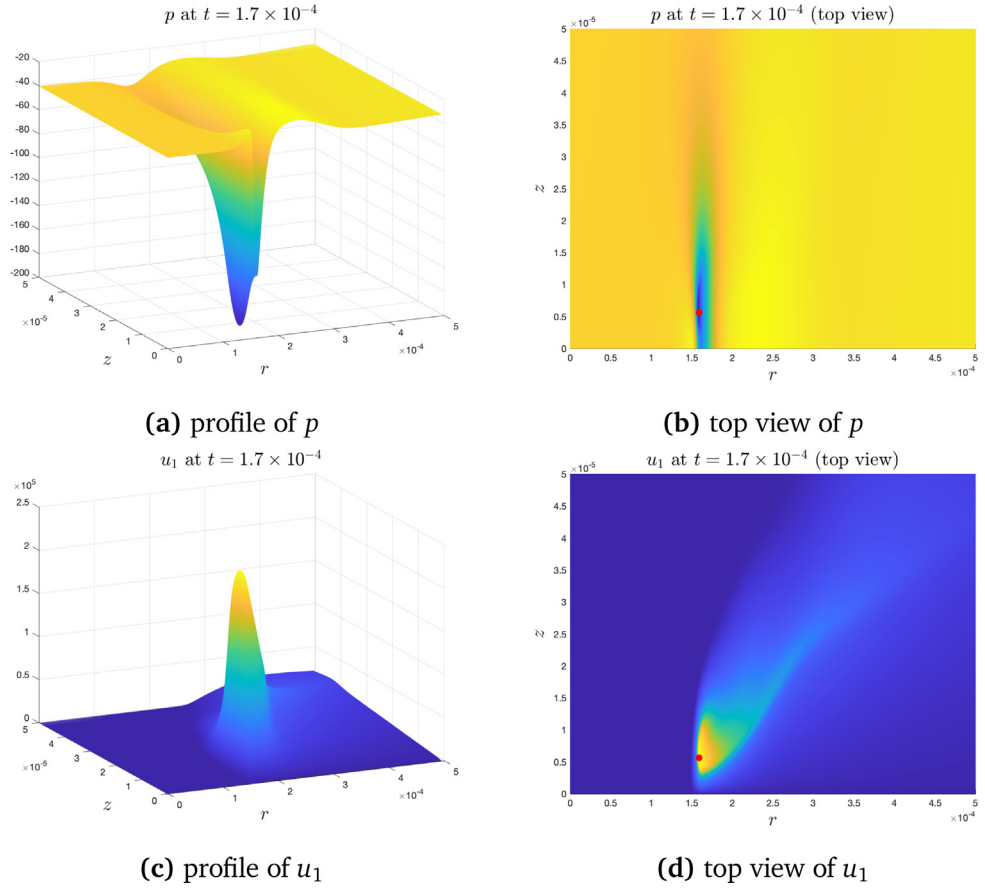

(a) profile of p **(b)** top view of p

(c) profile of u_1 **(d)** top view of u_1

Fig. 2.14. Profiles of p and u_1 at time $t = 1.7 \times 10^{-4}$. First row: profile and tow view of p. Second row: profile and top view of ω_1. The red point is the maximum location of u_1.

The change of the pressure in time also provides important indicators of potential blowup of the Navier–Stokes equations or the Euler equations. According to [28], if there is a blowup for the Navier–Stokes equations, the minimum of the normalized pressure p must tend to negative infinity at the singularity time, or the maximum of $|\boldsymbol{u}|^2/2 + p$ must tend to positive infinity. A recent result [29] states that the Hessian of p must grows faster than $O((T-t)^{-2})$ if the solution to the Euler equations is to blowup at time T. We thus also monitor the growth of the maximums of $-p$, $|\boldsymbol{u}|^2/2+p$ and $|D^2p|$ and plot them in Fig. 2.15. We can see that they all grow rapidly in time and faster than a double-exponential rate in the stable phase, which provides additional evidence for the potential two-scale singularity in our scenario. In particular, to check the blowup criterion with respect to the pressure Hessian, we need to fit the growth rate of $|D^2p|$ and compare it with $O((T-t)^{-2})$. We will perform careful fitting of growth rate of the solution in the following section.

2.8. Scaling properties of the solution

In this section, we will summarize some main findings of the scaling properties of the solution reported in [4]. In particular, we show that the growth and the spatial scaling of the solution obey some (inverse) power laws.

2.8.1. Linear fitting procedure

For a solution quantity $v(t)$ that is expected to blow up at some finite time T, a typical asymptotic model is the inverse power law:

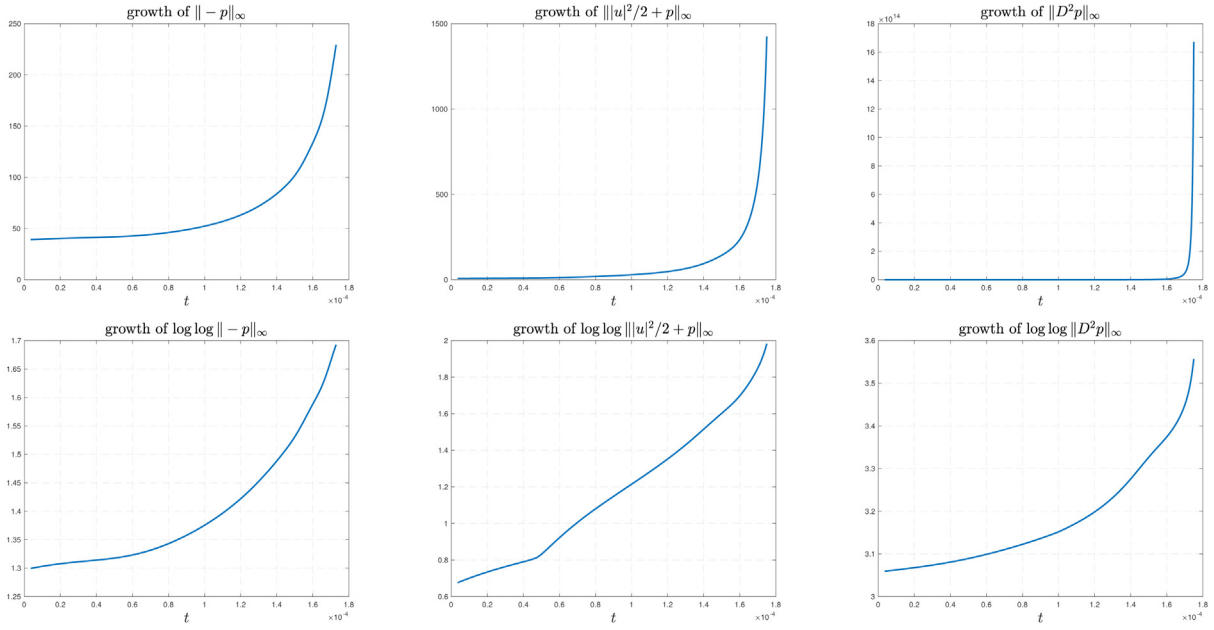

Fig. 2.15. First row: the growth of $\|-p\|_{L^\infty}$, $\||\boldsymbol{u}|^2/2+p\|_{L^\infty}$ and $\|D^2p\|_{L^\infty}$ as functions of time. Second row: $\log\log\|-p\|_{L^\infty}$, $\log\log\||\boldsymbol{u}|^2/2+p\|_{L^\infty}$ and $\log\log\|D^2p\|_{L^\infty}$.

$$v(t)\sim\alpha(T-t)^{-c_v}\quad\text{as}\quad t\to T, \tag{2.9}$$

where $c_v>0$ is the blowup rate and $\alpha>0$ is some constant. To verify that $v(t)$ satisfies an inverse power law and to learn the power c_v, we follow the idea of Luo and Hou [3] and study the time derivative of the logarithm:

$$\frac{\mathrm{d}}{\mathrm{d}t}\log v(t)=\frac{v'(t)}{v(t)}\sim\frac{c_v}{T-t}.$$

This naturally leads to the linear regression model

$$y(t;v):=\frac{v(t)}{v'(t)}\sim-\frac{1}{c_v}(t-T)=:\tilde{a}t+\tilde{b}, \tag{2.10}$$

with response variable y, explanatory variable t, and model parameters $\tilde{a}=-1/c_v$, $\tilde{b}=T/c_v$. The model (2.10) does not always yield an ideal fitting even if the inverse power law (2.9) does exist due to numerical errors and the use of adaptive mesh. To obtain a better approximation of c_v, we will conduct a local search near the crude estimate $\tilde{c}_v$ and find a value $\bar{c}_v$ such that the model

$$\gamma(t;v):=v(t)^{-1/\bar{c}_v}\sim\alpha^{-1/\bar{c}_v}(T-t)^{c_v/\bar{c}_v}\sim\alpha^{-1/c_v}(T-t)=:\bar{a}t+\bar{b} \tag{2.11}$$

has the best linear regression fitness (the R^2) against a least-square test.

2.8.2. Fitting of the growth rate

In [4], we have developed some effective fitting procedures to study the scaling properties of the numerical solutions obtained in our computation. Fig. 2.16 shows the fitting results for the quantity $\|u_1(t)\|_{L^\infty}$ on the time interval $[t_1,t_2]=[1.6\times10^{-4},1.75\times10^{-4}]$. We can see that both models, $y(t;\|u_1\|_{L^\infty})$ and $\gamma(t;\|u_1\|_{L^\infty})$, have excellent linear fitness with R^2 values very close to 1 (the R^2 value for the model $\gamma(t;\|u_1\|_{L^\infty})$ is greater than $1-10^{-6}$). The blowup rates and the blowup times inferred from the two models are close to each other, which cross-validate both models. This strongly implies that $\|u_1\|_{L^\infty}$ has a finite-time singularity of an inverse power law with a blowup rate very close to 1. Recall that $\psi_{1,z}(R(t),Z(t),t)\sim u_1(R(t),Z(t),t)$ in the stable phase $[1.6\times10^{-4},1.75\times10^{-4}]$. If we ignore the degenerate diffusion, then the equation of $\|u_1(t)\|_{L^\infty}$ can be approximated by

$$\frac{\mathrm{d}}{\mathrm{d}t}\|u_1(t)\|_{L^\infty}=2\psi_{1,z}(R(t),Z(t),t)\cdot u_1(R(t),Z(t),t)\sim c_0\|u_1(t)\|_{L^\infty}^2,$$

which then implies that $\|u_1(t)\|_{L^\infty}\sim(T-t)^{-1}$ for some finite time T. This asymptotic analysis is now supported by our linear fitting results.

Next, we study the growth of the maximum vorticity $\|\boldsymbol{\omega}\|_{L^\infty}$. We apply the fitting procedure to the maximums of the vorticity components instead of to the maximum vorticity. As an illustration, we present the study of the inverse power law of the axial vorticity component ω^z. Fig. 2.17 shows the linear fitting for the associated models of $\|\omega^z(t)\|_{L^\infty}$ on the time interval $[t_1,t_2]=[1.6\times10^{-4},1.75\times10^{-4}]$. We observe that both models $y(t;\|\omega^z\|_{L^\infty})$ and $\gamma(t;\|\omega^z\|_{L^\infty})$ have good linear fitness:

$$\|\omega^z(t)\|_{L^\infty}\sim(T-t)^{-\bar{c}_{\omega^z}},$$

with the estimated blowup rate approximately equal to 1.5. This implies that

$$\int_0^T\|\boldsymbol{\omega}(t)\|_{L^\infty}\geq\int_0^T\|\omega^z(t)\|_{L^\infty}\,\mathrm{d}t=+\infty.$$

This provides strong numerical evidence of a finite-time singularity of the solution to the initial–boundary value problem (2.2)–(2.5).

As mentioned in Section 2.7, the unbounded growth of the pressure and related quantities may also indicate the existence of a potential finite singularity. We thus also performed linear fitting for the quantities $\|p\|_{L^\infty}$, $\||\boldsymbol{u}|^2/2+p\|_{L^\infty}$, $\|D^2p\|_{L^\infty}$ and obtained the following inverse power law fitting:

$$\|p\|_{L^\infty}\sim(T-t)^{-1},\quad\||\boldsymbol{u}|^2/2+p\|_{L^\infty}\sim(T-t)^{-1.28},$$
$$\|D^2p\|_{L^\infty}\sim(T-t)^{-2.4}$$

The linear regression of the associated γ models are shown in Fig. 2.18. The inverse power laws of $\|p\|_{L^\infty}$ and $\||\boldsymbol{u}|^2/2+p\|_{L^\infty}$ imply that the no-blowup criteria in [28] are violated, and thus a finite time singularity may exist. Moreover, the estimated blowup power of $\|D^2p\|_{L^\infty}$ being greater than 2 violates the no-blowup

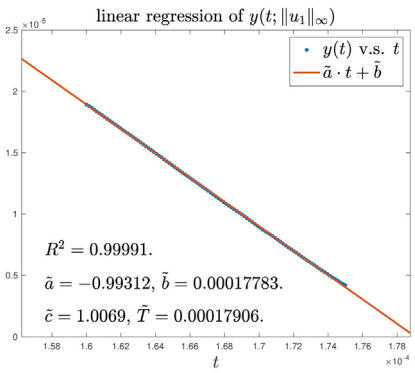

(a) linear regression of $\|u_1(t)\|_{L^\infty} / \|u_1(t)\|'_{L^\infty}$

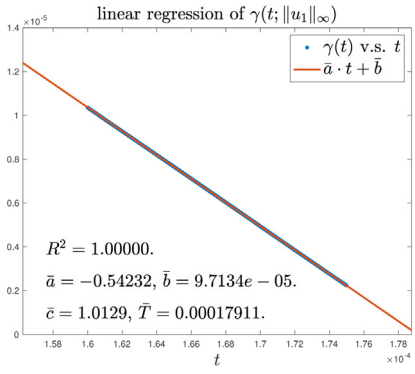

(b) linear regression of $\|u_1(t)\|_{L^\infty}^{1/\bar{c}_{u_1}}$

Fig. 2.16. The linear regression of (a) $y(t; \|u_1\|_{L^\infty})$ and (b) $\gamma(t; \|u_1(t)\|_{L^\infty})$ on the time interval $[t_1, t_2] = [1.6 \times 10^{-4}, 1.75 \times 10^{-4}]$. The blue points are the data points obtained from our computation, and the red lines are the linear models. We plot the linear models on a larger interval.

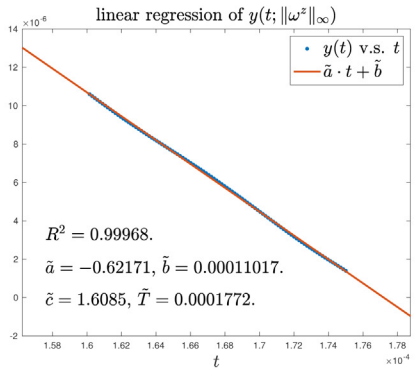

(a) linear regression of $\|\omega^z(t)\|_{L^\infty} / \|\omega^z(t)\|'_{L^\infty}$

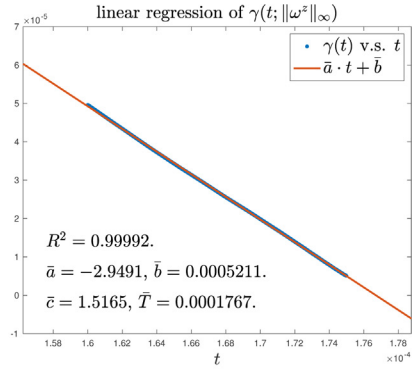

(b) linear regression of $\|\omega^z(t)\|_{L^\infty}^{1/\bar{c}_{\omega^z}}$

Fig. 2.17. The linear regression of (a) $y(t; \|\omega^z\|_{L^\infty})$ and (b) $\gamma(t; \|\omega^z\|_{L^\infty})$ on the time interval $[t_1, t_2] = [1.6 \times 10^{-4}, 1.75 \times 10^{-4}]$. The blue points are the data points obtained from our computation, and the red lines are the linear models. We plot the linear models on a larger interval.

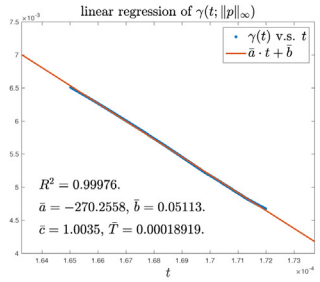

(a) fitting regression of $\|p\|_{L^\infty}$

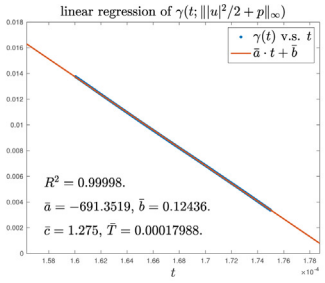

(b) fitting of $\||u|^2/2 + p\|_{L^\infty}$

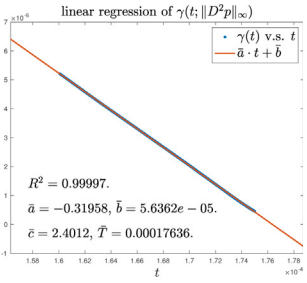

(c) fitting of $\|D^2 p\|_{L^\infty}$

Fig. 2.18. The linear regression of (a) $\gamma(t; \|p\|_{L^\infty})$, (b) $\gamma(t; \||\boldsymbol{u}|^2/2 + p\|_{L^\infty})$ and (c) $\gamma(t; \|D^2 p\|_{L^\infty})$ as functions of time. The blue points are the data points obtained from our computation, and the red lines are the linear models. We plot the linear models on a larger interval.

criterion in [29], further supporting the potential finite time blowup trend.

2.8.3. Fitting of spatial scales

Similarly, we can perform linear fitting for the two spatial scales of the solution $R(t)$ and $Z(t)$:

$$R(t) = (T - t)^{c_s}, \quad Z(t) = (T - t)^{c_l}. \tag{2.12}$$

We obtain the following power law fitting:

$$R(t) \sim (T - t)^{0.5}, \quad Z(t) \sim (T - t). \tag{2.13}$$

Fig. 2.19 presents the linear regression of model (2.11) for $R(t)^{-1}$, $Z(t)^{-1}$. We can see in Fig. 2.19(a) that $R(t)$ has an excellent fitting to a power law with a rate $\bar{c}_s \approx 0.5$. Fig. 2.19(b) shows that $Z(t)$ also approximately satisfies the power law with a rate $\bar{c}_l \approx 1$. We also observe that the fitness of $Z(t)$ is not as good as that of $R(t)$,

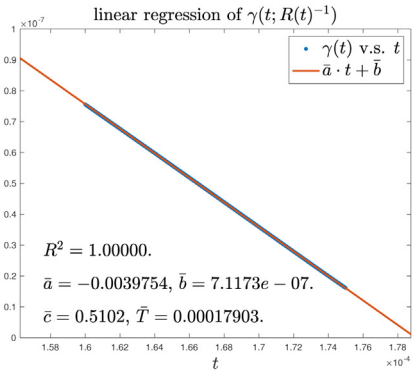

(a) linear regression of $R(t)^{1/\bar{c}_s}$

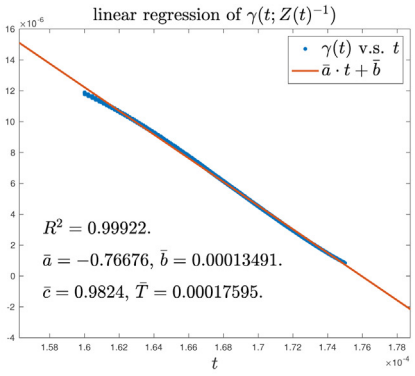

(b) linear regression of $Z(t)^{1/\bar{c}_l}$

Fig. 2.19. The linear regression of (a) $\gamma(t; R(t)^{-1})$ and (b) $\gamma(t; Z(t)^{-1})$ on the time interval $[t_1, t_2] = [1.6 \times 10^{-4}, 1.75 \times 10^{-4}]$. The blue points are the data points obtained from our computation, and the red lines are the linear models. We plot the linear models on a larger interval.

which may be due to the fact that the numerical recording of $Z(t)$ is sensitive to the adaptive mesh and the interpolation operation between different meshes.

2.9. Numerical evidence of locally self-similar profiles

It is well known that the 3D Euler equations have the scaling invariance property that, if $\boldsymbol{u}(x, t)$ is a solution to the equations, then

$$\boldsymbol{u}_{\lambda,\tau}(x, t) := \frac{\lambda}{\tau}\boldsymbol{u}\left(\frac{x}{\lambda}, \frac{t}{\tau}\right), \quad \forall \lambda, \tau \in \mathbb{R},$$

is still a solution. Similarly, the 3D Navier–Stokes equations satisfy a more restricted scaling invariance property that, if $\boldsymbol{u}(x, t)$ is a solution to the equations, then

$$\boldsymbol{u}_{\lambda}(x, t) := \frac{1}{\lambda}\boldsymbol{u}\left(\frac{x}{\lambda}, \frac{t}{\lambda^2}\right), \quad \forall \lambda \in \mathbb{R},$$

is still a solution. Regarding these scaling properties, a fundamental question is whether the Euler equations or the Navier–Stokes equations have self-similar solutions of the form

$$\boldsymbol{u}(x, t) = \frac{1}{(T-t)^{\gamma}}\boldsymbol{U}\left(\frac{x - x_0}{(T-t)^{\beta}}\right), \tag{2.14}$$

where $\boldsymbol{U}$ is a self-similar vector profile and $\beta, \gamma > 0$ are scaling exponents. If such a solution exists, it will imply that the Euler equations or the Navier–Stokes equations can develop a focusing self-similar singularity at the point x_0 at a finite time T.

We remark that these scaling properties of the Euler equations or the Navier–Stokes equations cannot hold globally in our scenario due to the existence of the cylinder boundary at $r = 1$ and the variable diffusion coefficients. Nevertheless, a focusing self-similar blowup can still exist asymptotically and locally near the symmetry axis $r = 0$. Below we provide some numerical evidence on the existence of locally self-similar profiles in a small-scale neighborhood of $(R(t), Z(t))$, the maximum location of u_1. More detailed scaling analysis and scaling properties can be found in [4].

Fig. 2.20 compares the level sets of u_1 at different time instants. The first row of Fig. 2.20 plots the level sets of u_1 in a local domain $(r, z) \in [0.8 \times 10^{-4}, 2.5 \times 10^{-4}] \times [0, 8 \times 10^{-6}]$. We can see that in a short time interval, from $t = 1.72 \times 10^{-4}$ to $t = 1.75 \times 10^{-4}$, the profile of u_1 has changed a lot. The support of the profile shrinks in space and travels towards the origin. The sharp front also becomes thinner and thinner. In the second row of Fig. 2.20, we plot the level sets of the spatially rescaled function

$$\tilde{u}_1(\xi, \zeta, t) = u_1(Z(t)\xi + R(t), Z(t)\zeta, t).$$

We can see that the landscape of $\tilde{u}_1$ (in the $\xi\zeta$-plane) almost does not change in this time interval. Here

$$\xi = \frac{r - R(t)}{Z(T)} \sim \frac{r - R(t)}{(T-t)^{c_l}}, \quad \zeta = \frac{z}{Z(T)} \sim \frac{z}{(T-t)^{c_l}}$$

are dynamically rescaled variables. This observation provides strong evidence on the existence of a self-similar profile $U(\xi, \zeta)$ for u_1.

In Fig. 2.21, we compare the level sets of ω_1 and the level sets of the spatially rescaled function

$$\tilde{\omega}_1(\xi, \zeta, t) = \omega_1(Z(t)\xi + R(t), Z(t)\zeta, t)$$

in a similar manner. Again, we can see that this profile of ω_1 has changed a lot in the time interval $t \in [1.72 \times 10^{-4}, 1.75 \times 10^{-4}]$, while the spatially rescaled profile $\tilde{\omega}_1$ seems to converge. This provides strong evidence on the existence of a self-similar profile $\Omega(\xi, \zeta)$ for ω_1.

3. The Euler equations with time-dependent vanishing numerical viscosity

In this section, we study a new scenario of computation for the 3D impressible Euler equations. In particular, we investigate the potential two-scale singularity for the 3D axisymmetric Euler equations with time-dependent vanishing numerical viscosity. Our computational results imply that the 3D Euler equations may also develop a two-scale traveling wave singularity with the same initial data as in the previous section.

3.1. Description of the problem

As reported in [4], the 3D axisymmetric Euler equations may develop a traveling wave singularity that is qualitatively similar to the potential two-scale singularity of the Navier–Stokes equations with degenerate diffusion. However, without any regularization of viscosity, the Euler equations quickly developed a very thin structure near the sharp front whose thickness collapses to zero even faster than the scale of $Z(t)$. This extra small scale in the solution of the 3D Euler equations is extremely difficult to resolve numerically, and thus the computation of the potential blowup cannot reach to a stable phase.

In order to study the potential singularity of the 3D Euler equations in a similar scenario for a longer time, we consider to solve the Euler equations with time-dependent vanishing numerical viscosity that may regularize the extra scale. That is, we still consider the equations of the form (2.1) while the diffusion coefficient ν now represents the numerical viscosity that vanishes

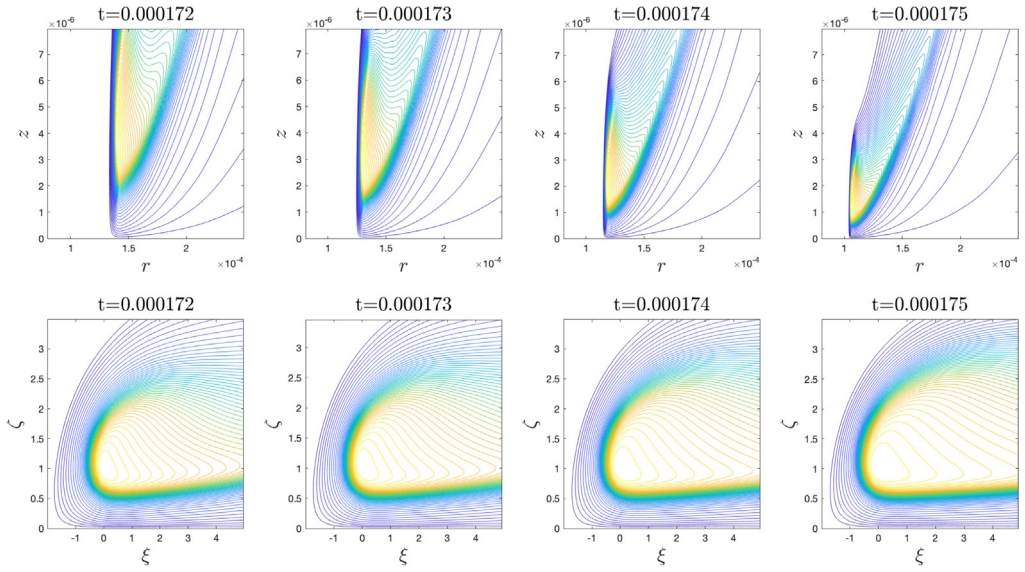

Fig. 2.20. Comparison of the level sets of u_1 at different time instants. First row: original level sets of u_1 in the domain $(r, z) \in [0.8 \times 10^{-4}, 2.5 \times 10^{-4}] \times [0, 8 \times 10^{-6}]$. Second row: rescaled level sets of u_1 as a function of (ξ, ζ) in the domain $(\xi, \zeta) \in [-2, 5] \times [0, 3.5]$.

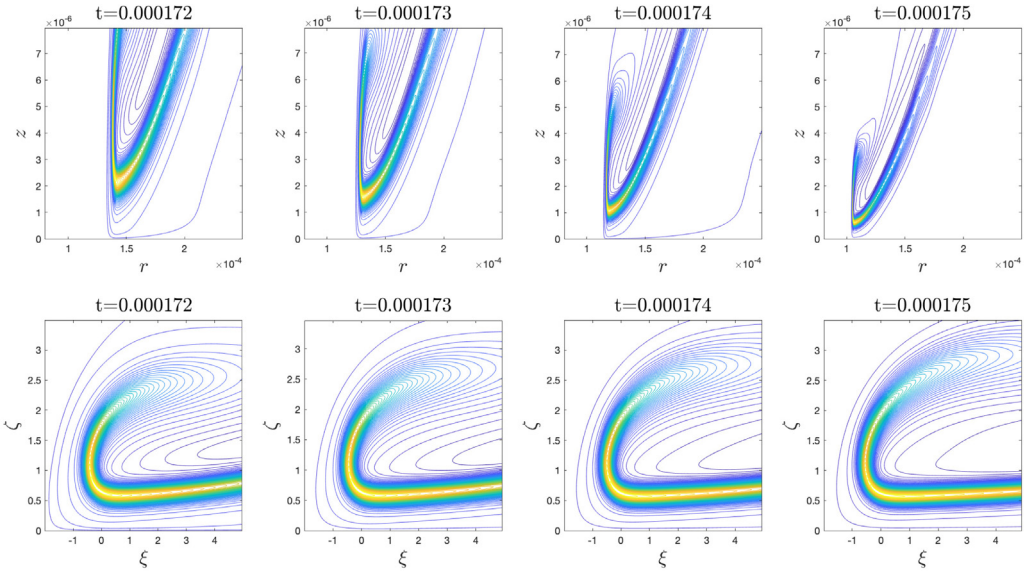

Fig. 2.21. Comparison of the level sets of ω_1 at different time instants. First row: original level sets of u_1 in the domain $(r, z) \in [0.8 \times 10^{-4}, 2.5 \times 10^{-4}] \times [0, 8 \times 10^{-6}]$. Second row: rescaled level sets of ω_1 as a function of (ξ, ζ) in the domain $(\xi, \zeta) \in [-2, 5] \times [0, 3.5]$.

in time and depends on the resolution (mesh size) of the numerical solution. In the cylindrical coordinates and in terms of the transformed variables u_1, ω_1, ψ_1, the equations we solve in this section are

$$u_{1,t} + u^r u_{1,r} + u^z u_{1,z} = 2u_1\psi_{1,z} + g_{u_1}, \tag{3.1a}$$

$$\omega_{1,t} + u^r \omega_{1,r} + u^z \omega_{1,z} = 2u_1 u_{1,z} + g_{\omega_1}, \tag{3.1b}$$

$$-\left(\partial_r^2 + \frac{3}{r}\partial_r + \partial_z^2\right)\psi_1 = \omega_1, \tag{3.1c}$$

$$u^r = -r\psi_{1,z}, \quad u^z = 2\psi_1 + r\psi_{1,r}, \tag{3.1d}$$

where numerical diffusion terms g_{u_1}, g_{ω_1} are given by

$$g_{u_1} = \nu^r\left(u_{1,rr} + \frac{3}{r}u_{1,r}\right) + \nu^z u_{1,zz}, \tag{3.2a}$$

$$g_{\omega_1} = \nu^r\left(\omega_{1,rr} + \frac{3}{r}\omega_{1,r}\right) + \nu^z \omega_{1,zz}. \tag{3.2b}$$

Note that the formulas in (3.2) are much simpler than those in (2.3) because ν^r, ν^z are now constants in space at each time instant.

3.1.1. Vanishing numerical diffusion coefficient

In this scenario, the diffusion coefficients ν^r, ν^z are chosen to be only functions of time:

$$\nu^r(t) = 256h \cdot \left(\frac{10R(t)^2}{1 + 10^8 R(t)^2} + \frac{10^2(\sin(\pi Z(t))/\pi)^2}{1 + 10^{11}(\sin(\pi Z(t))/\pi)^2}\right), \tag{3.3a}$$

$$\nu^z(t) = 256h \cdot \left(\frac{10^{-1}R(t)^2}{1 + 10^8 R(t)^2} + \frac{10^4(\sin(\pi Z(t))/\pi)^2}{1 + 10^{11}(\sin(\pi Z(t))/\pi)^2}\right), \tag{3.3b}$$

where $(R(t), Z(t))$ is the maximum location of u_1 and h is a mesh parameter proportional to the computational grid size.

There are two major reasons for choosing the diffusion coefficients in the form above. First of all, we want the numerical viscosity to mimic the effect of the degenerate diffusion coefficients in the previous scenario, especially in the small blowup region around the point $(R(t), Z(t))$. As discussed in [4], the degenerate diffusion coefficients plays a critical role in the stable development of the potential two-scale singularity reviewed in Section 2. Therefore, part of the numerical diffusion coefficients ν^r, ν^z are constructed using exactly the same formulas as in (2.7) with the spatial coordinates r, z replaced by the time-dependent parameters $R(t), Z(t)$, so that they have the same dynamic scaling properties as those for the degenerate diffusion coefficients (2.7) near the center of the traveling wave, $(R(t), Z(t))$. Note that ν^r, ν^z vanish in time if $R(t), Z(t)$ converge to 0 as in the previous scenario.

Secondly, we want the numerical viscosity to tend to zero as the numerical resolution of the solution goes to infinity. In this way, the numerical solution may converge to the solution of the original Euler equations as we refine the resolution by reducing the grid size. However, we also do not want the numerical viscosity to converge to zero too fast such that it is too weak to control the Euler instability at a finite resolution. This is why we add a factor of h (rather than h^2) to the time-dependent diffusion coefficients ν^r, ν^z. In particular, we choose $h = 1/m$ where m is the number of the mesh points in the z direction, so the overall numerical viscosity is of first order.

3.1.2. Initial–boundary value problem

We will solve the transformed equations (3.1) in the cylinder region $\mathcal{D} = \{(r, z) : 0 \le r \le 1\}$ using the same initial data (2.5) and the same boundary conditions as described in 2.1. That is, the only difference in the current problem is the choice of the diffusion coefficients. As we will see, the solution to the 3D axisymmetric Euler equations with the new vanishing numerical viscosity will develop a two-scale traveling wave blowup that is qualitatively similar to that of the Navier–Stokes equations with spatially degenerate diffusion coefficients. Such potential blowup phenomenon is robust as we refine the resolution (so that the numerical viscosity is weaker), implying that the original 3D axisymmetric Euler equations may also develop a traveling wave singularity with the same features.

Since the problem setting is almost the same as before, we will employ the same numerical method in [4] to solve the initial–boundary value problem. Moreover, in addition to the first order numerical viscosity (3.2), we also apply a first order low pass filtering to control the strong Euler instability along the thin tail of the solution. Therefore, the overall algorithm is first order in space and second order in time. We have also performed careful convergence to confirm that our numerical method is indeed first order convergent.

For convenience, we will refer the computation of the Navier–Stokes equations with degenerate diffusion coefficient (Section 2) as Case I and the computation of the Euler equations with first order vanishing diffusion coefficient as Case II.

3.2. Profile evolution

In this subsection, we study the evolution of the solution in Case II. We will compare the numerical results with those of Case I and of the original Euler equations. We will also compare the computations in Case II of different resolutions as the grid size determines the strength of the numerical viscosity. When the resolution is not specified, we assume to use the results computed with mesh size 1024×512, in which case the factor $256h$ equals to 0.5.

We have computed the numerical solution up to time $t = 1.75 \times 10^{-4}$ when it is still well resolved. As in Case I, the computation in Case II also has a warm-up phase and a stable phase but with a earlier transition time. In the warm-up phase ($t \in [0, 1.56\times 10^{-4}]$), the solution evolves from the smooth initial data into a special structure that is qualitatively similar to the solution in Case I. In the stable phase ($t \in (1.56 \times 10^{-4}, 1.75 \times 10^{-4}]$), the solution again maintains the special geometric structure and blows up stably. The overall behavior of the solution in Case II is almost identical to that of Case I, implying that the modification in the diffusion terms does not harm the potential blowup trend.

Fig. 3.1 plots the solution u_1, ω_1 in the rectangular domain $\{(r, z) : 0 \le r \le 10^{-3}, 0 \le z \le 10^{-4}\}$ and the square domain $\{(r, z) : 0 \le r \le 10^{-3}, 0 \le z \le 10^{-3}\}$ at time $t = 1.63 \times 10^{-4}$. One may compare it with Figs. 2.2, 2.5 and see that the solution shares almost the same geometric features of that in Case I. The solution again forms a thin structure in the z direction, a sharp front in the r direction, and a long tail part propagating towards the far field. There is a "vacuum" region between the sharp front and the symmetry axis where the velocity field has almost no angular component. The high contrast between the scale of the thin structure and the scale of the vacuum region again characterizes the two-scale feature of the solution.

A closer look of the solution in a local region around $(R(t), Z(t))$ is presented in Fig. 3.2. The solution profiles are still very smooth with respect to the smaller scale $Z(t)$. By comparing Fig. 3.2 with Fig. 2.6 we can also see that the solution structure near the front in Case II is basically the same as in Case I: the profile of u_1 develops a "two-phase" feature and the profile of ω_1 forms a thin structure that behaves like a regularized 1D delta function supported along the "boundary" of u_1.

We compare in Fig. 3.3 the trajectories of $(R(t), Z(t))$ (the maximum location of u_1) for Case I, Case II and the original Euler case. Since the resolution affects the numerical viscosity in Case II, we thus present two results in Case II with different mesh sizes. As reported in [4], the original Euler equations with the same initial data can only be resolved before 1.6×10^{-4}. We therefore have no trustworthy data for the Euler equations in the stable phase. Nevertheless, the four trajectories seem to agree with each other qualitatively over the whole computation. The ratio between the two scales $(R(t)/Z(t))$, however, reflects the effect of different diffusion coefficients. The vanishing diffusion coefficients in Case II is relatively smaller than the degenerate diffusion coefficients near $(R(t), Z(t))$ due to the factor $256h$ that is proportional to grid size. Fig. 3.3 thus shows that the contrast between the two scales $R(t)$ and $Z(t)$ becomes larger as the diffusion becomes weaker, which implies that the Euler solution, if can be continued to a later time, may develop a much stronger two-scale feature. This also suggests that the potential two-scale blowup is intrinsic to the Euler equations in this special scenario rather than an artifact of the specific diffusion coefficients.

We remark that the structure and magnitude distribution of the 2D flow field (u^r, u^z) in Case II are also qualitatively similar to those in Case I. We thus do not visualize the 2D flow field in Case II to avoid redundancy.

The pressure function also develops a deep well in Case II as shown in Fig. 3.4, and the location of the pressure well again aligns with the peak of u_1. One should compare Fig. 3.4 with Fig. 2.14 and see that the pressure forms a similar profile in Case I and Case II. Yet a more careful look reveals that the pressure well is deeper in Case II than in Case I at the same time instant, due to a decrease in the strength of the viscosity. As we discussed in Section 2.7, the low pressure well contributes to the formation of the two-phase feature of u_1, as it prevents the fluid with high angular velocity from escaping the low pressure region around $(R(t), Z(t))$. The sharp jump of the pressure in the r direction

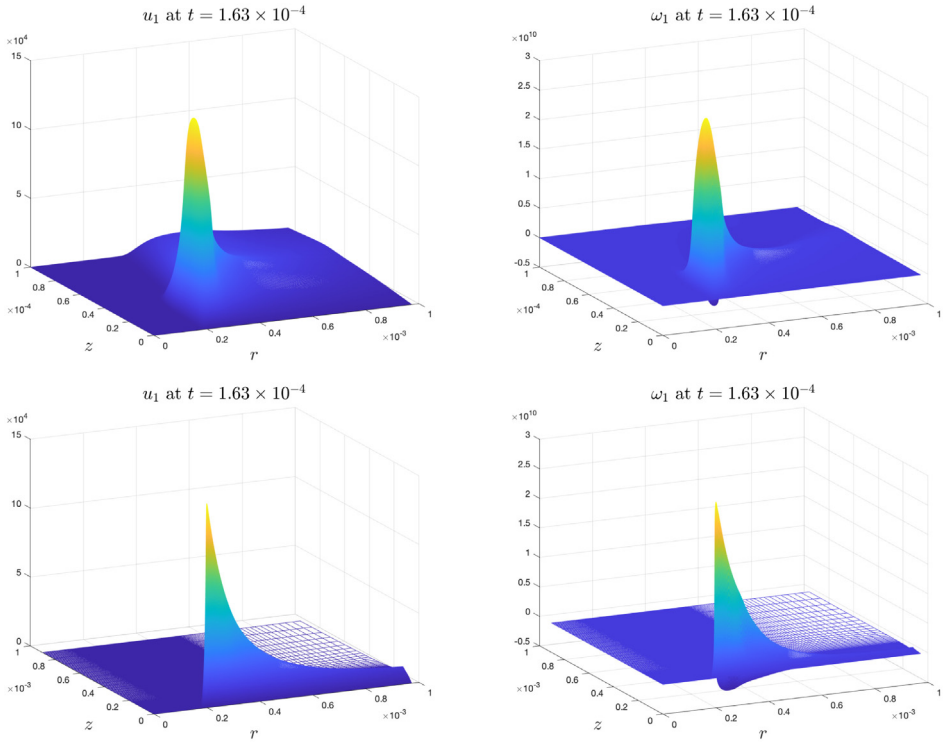

Fig. 3.1. First row: profiles of u_1, ω_1 at $t = 1.63 \times 10^{-4}$ in the rectangular domain $\{(r, z) : 0 \le r \le 10^{-3}, 0 \le z \le 10^{-4}\}$. Second row: in the square domain $\{(r, z) : 0 \le r \le 10^{-3}, 0 \le z \le 10^{-3}\}$.

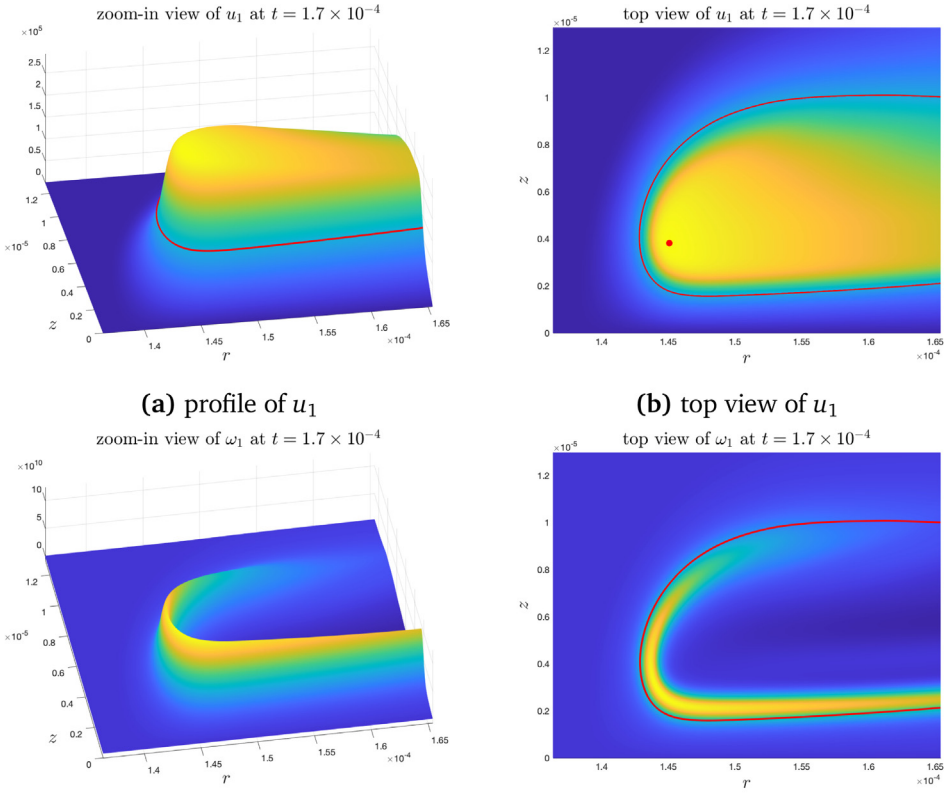

(a) profile of u_1 **(b)** top view of u_1

(c) profile of ω_1 **(d)** top view of ω_1

Fig. 3.2. Zoom-in views of u_1, ω_1 at time $t = 1.7 \times 10^{-4}$. First row: profile and tow view of u_1. Second row: profile and top view of ω_1. The red curve (in all figures above) is the level set of u_1 for the value $0.3\|u_1\|_{L^\infty}$, and the red point is the maximum location of u_1.

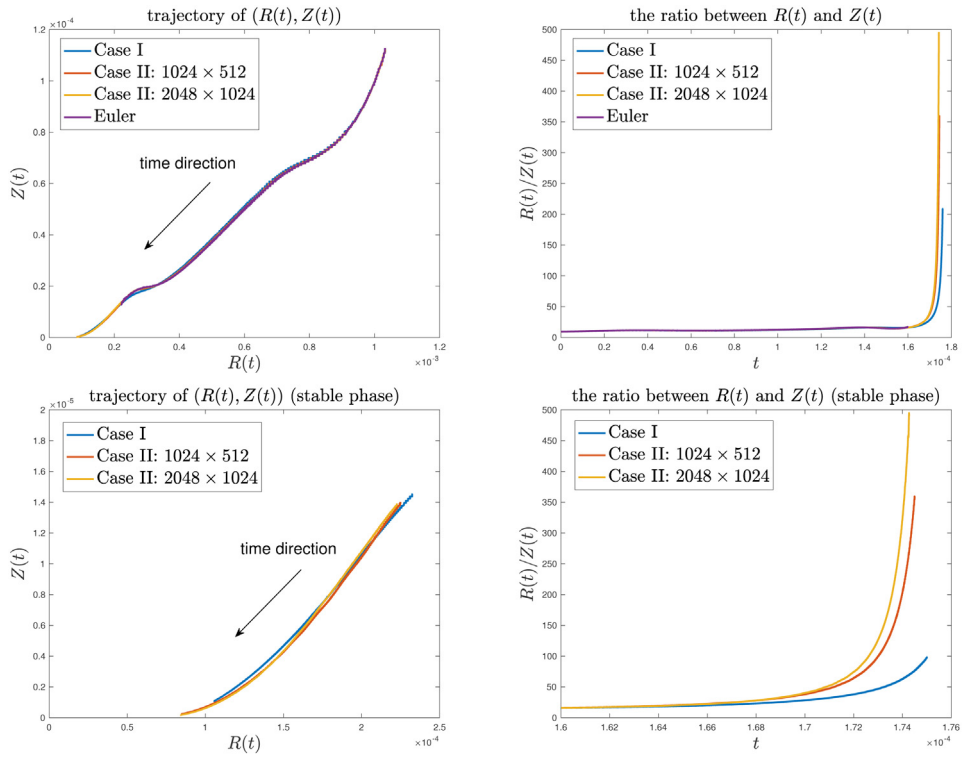

Fig. 3.3. The trajectory of $(R(t), Z(t))$ and the ratio $R(t)/Z(t)$ as a function of time. First row: the whole computation. Second row: the stable phase.

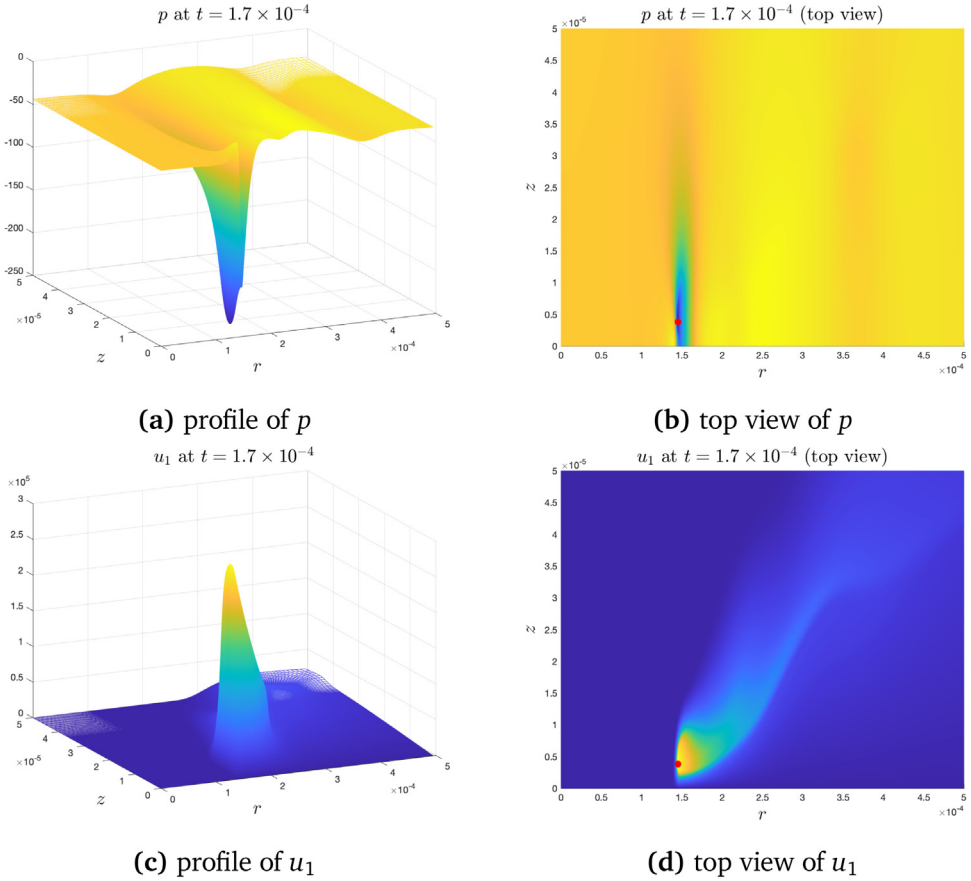

(a) profile of p **(b)** top view of p

(c) profile of u_1 **(d)** top view of u_1

Fig. 3.4. Profiles of p and u_1 at time $t = 1.7 \times 10^{-4}$. First row: profile and tow view of p. Second row: profile and top view of ω_1. The red point is the maximum location of u_1.

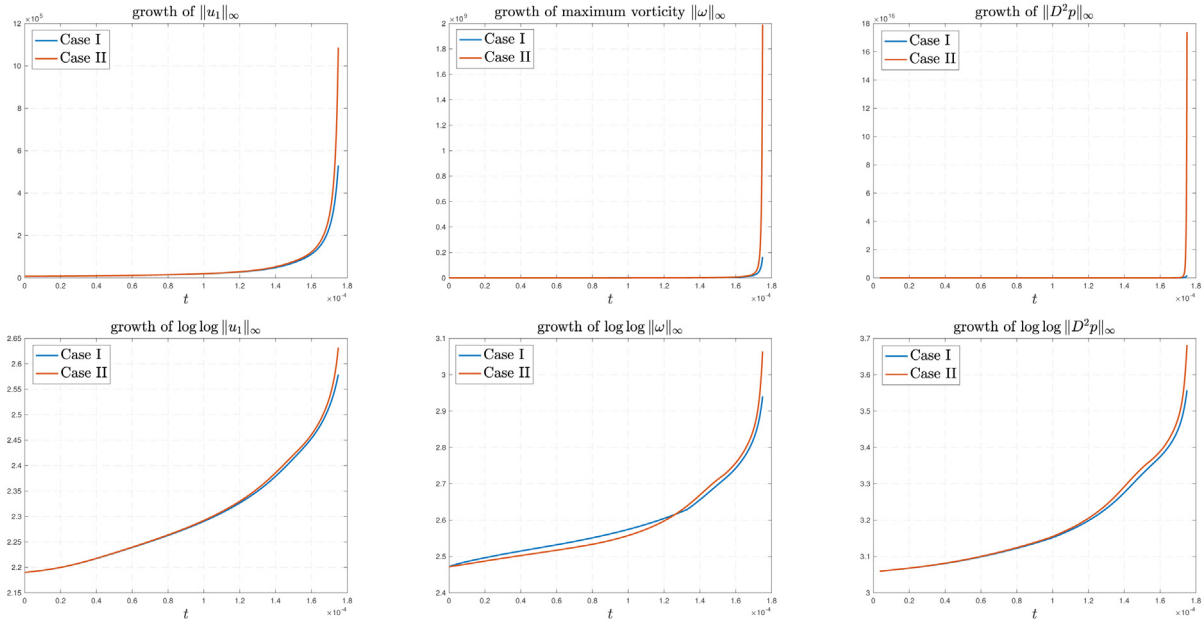

Fig. 3.5. First row: the growth of $\|u_1\|_{L^\infty}$, $\|\boldsymbol{\omega}\|_{L^\infty}$ and $\|D^2p\|_{L^\infty}$ as functions of time. Second row: $\log\log\|u_1\|_{L^\infty}$, $\log\log\|\boldsymbol{\omega}\|_{L^\infty}$ and $\log\log\|D^2p\|_{L^\infty}$.

yields a strong force pushing against the traveling wave of the solution, thus resulting in a sharp front in the solution profile.

3.3. Faster growth

We have seen that modifying the diffusion coefficient from a spatially degenerate function to a time-dependent vanishing parameter does not destroy or change the major features of the potential two-scale blowup. In fact, we can also observe the rapid growth of the solution in this new scenario, and the growth of the solution in Case II is faster than that in Case I. Fig. 3.5 compares the growth of $\|u_1\|_{L^\infty}$, $\|\boldsymbol{\omega}\|_{L^\infty}$, $\|D^2p\|_{L^\infty}$ in Case I and Case II. One can see that the vanishing numerical viscosity in Case II results in a faster growth of these quantities than in Case I. Recall that the rapid growth of $\|\boldsymbol{\omega}\|_{L^\infty}$ suggests a finite time blowup for the Euler equations according the Beale–Kata–Majda criteria [6], and the rapid growth of $\|D^2p\|_{L^\infty}$ relates to a potential finite time blowup via the criteria recently introduced in [29].

In order to predict the solution growth in the Euler limit, we also compare the growth rates of the maximum vorticity $\|\boldsymbol{\omega}\|_{L^\infty}$ for different resolutions in Case II and for the original Euler equations. Again, the Euler result is only presented up to $t = 1.6 \times 10^{-4}$ when it is still resolved. As shown in Fig. 3.6, the finer the resolution is, the faster the solution grows, and the Euler solution grows the fastest before $t = 1.6 \times 10^{-4}$. Moreover, the growth curve of $\|\boldsymbol{\omega}\|_{L^\infty}$ seems to converge and approach the Euler case as the resolution is refined. Therefore, it is reasonable to believe that the original Euler solution, if can be continued beyond $t = 1.6 \times 10^{-4}$, should blow up even faster than the solution in Case I or Case II.

Moreover, we have also tested the solution in Case I against the Constantin–Fefferman–Majda non-blowup criterion [9] for the 3D Euler equations. It asserts that the solution cannot blowup if the velocity field $\boldsymbol{u}$ is uniformly bounded and the local vorticity direction $\boldsymbol{\xi} = \boldsymbol{\omega}/|\boldsymbol{\omega}|$ is sufficiently "well behaved" near the region of maximum vorticity. In particular, the "well behaving" condition for the vorticity direction $\boldsymbol{\xi}$ up to a finite time T requires that the integral $\int_0^T \|\nabla\boldsymbol{\xi}\|_{L^\infty(B_t)}\,dt$ is bounded for some time-dependent neighborhood B_t of the maximum location of $|\boldsymbol{\omega}|$. In the original statement of this non-blowup condition, the evolution of the set B_t corresponds to the Lagrangian flow map induced by the velocity field $\boldsymbol{u}$, which is not easy to track accurately using our current numerical method. We thus choose to check a variant of the Constantin–Fefferman–Majda criterion by monitoring the growth of maximum $|\nabla\boldsymbol{\xi}|$ over the dynamic set $\Omega_t = \{(r,z) : |\boldsymbol{\omega}(r,z,t)| \geq \frac{1}{2}\|\boldsymbol{\omega}\|_{L^\infty}\}$. Fig. 3.7(a) shows that the quantity $\|\nabla\boldsymbol{\xi}\|_{L^\infty(\Omega_t)}$ grows rapidly after $t = 1.6 \times 10^{-4}$. Later in Section 3.5, a numerical fitting of the growth rate of $\|\nabla\boldsymbol{\xi}\|_{L^\infty(\Omega_t)}$ suggests that the integral $\int_0^T \|\nabla\boldsymbol{\xi}\|_{L^\infty(\Omega_t)}\,dt$ shall become unbounded for some finite time T, implying that a variant of the Constantin–Fefferman–Majda criterion is violated. Fig. 3.7(b) plots the 2D vector field of (ω^r, ω^z) in a rescaled neighborhood of the maximum location of $|\boldsymbol{\omega}|$ (indicated by the blue dot) at the time instant $t_0 = 1.7 \times 10^{-4}$. We can see that the partial vorticity field (ω^r, ω^z) has a twisted structure near the maximum location of $|\boldsymbol{\omega}|$, which also suggests a potential singular behavior of the solution according to the Constantin–Fefferman–Majda criterion.

3.4. Potential blowup mechanism

In Section 2.6, we summarize the blowup mechanism for the potential two-scale singularity in Case I. Since the solution to the Euler equations with vanishing numerical viscosity evolves in a qualitatively similar way as in Case I, we should expect that the previous blowup mechanism also applies in Case II.

That is, the odd symmetry and thin structure of u_1 in the z direction yields a sharp gradient $(u_1^2)_z$ near $z = 0$, which constitutes to the rapid growth of ω_1 via the ω_1 Eq. (3.1b). A larger ω_1 induces a stronger local flow with u^r pointing towards the axis $r = 0$, which generates a larger positive value of $\psi_{1,z} = -u^r/r$ near $(r,z) = (R(t), 0)$. The growth of $\psi_{1,z}$ then accelerates the growth of u_1 via the vortex stretching term $2\psi_{1,z}u_1$. The decreasing trend of $\psi_{1,z}$ as a function of z also induces a traveling wave for u_1 propagating towards $z = 0$, which generates an even sharper gradient of u_1 in z. This positive feedback loop is summarized in (2.8). In the mean time, the negative radial velocity field u^r pushes the solution towards the axis $r = 0$, resulting in a traveling wave in the r direction. Since the shrinking in the z direction is induced by the vortex stretching rather than the advection, the structure

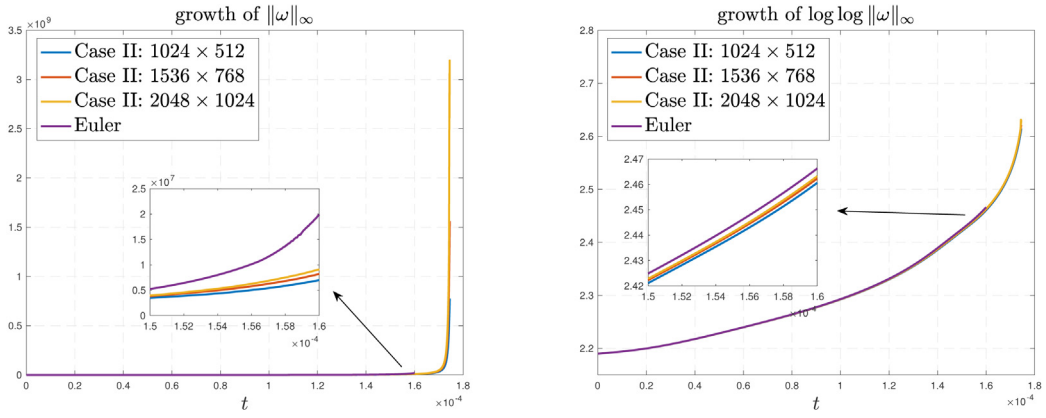

Fig. 3.6. Growth of $\|\boldsymbol{\omega}\|_{L^\infty}$ for different resolutions in Case II and for the original Euler equations.

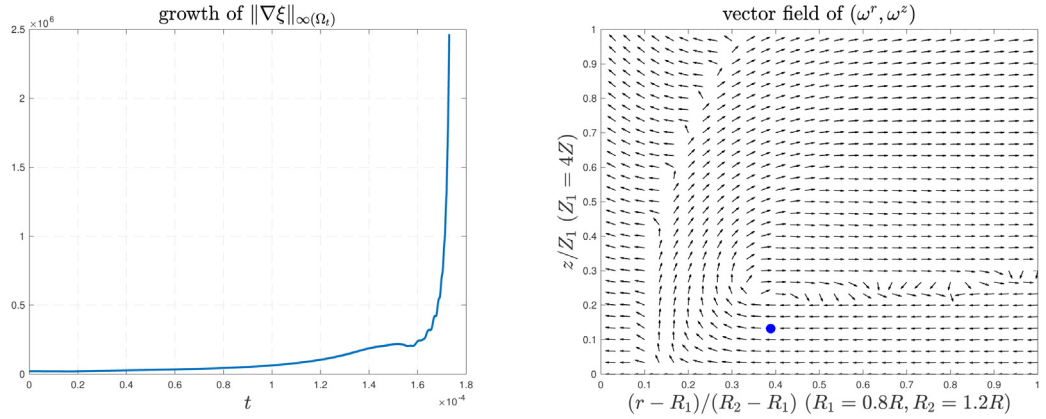

(a) growth of $\|\nabla\boldsymbol{\xi}\|_{L^\infty(\Omega_t)}$ **(b)** partial vorticity field (ω^r, ω^z)

Fig. 3.7. (a) The growth of $\|\nabla\boldsymbol{\xi}\|_{L^\infty(\Omega_t)}$ in time. (b) The partial vorticity field (ω^r, ω^z) in a rescaled domain at $t = 1.7 \times 10^{-4}$. The blue dot is the maximum location of $|\boldsymbol{\omega}|$, and the reference coordinate (R, Z) is the maximum location of u_1.

of the solution in z is much thinner, inducing a two-scale solution structure.

The good alignment between u_1 and $\psi_{1,z}$ is a critical part of this blowup mechanism. We illustrate this alignment in Case II in Fig. 2.13. One can see that the spatial alignment between u_1, $\psi_{1,z}$ is almost the same as in Case I, and $\psi_{1,z}$ is again comparable to u_1 in magnitude around $(R(t), Z(t))$ in the stable phase. This strong quadratic alignment leads to the rapid growth of u_1 and drags $Z(t)$ towards $z = 0$. In particular, it implies that maximum u_1 should blow up like $(T-t)^{-1}$ for some finite time T. In Fig. 3.8(c), we plot the ratio $\psi_{1,z}/u_1$ at the point $(R(t), Z(t))$ as a function of time for different cases and we have the following observations. Firstly, all the alignment curves look qualitatively similar, while the curves in Case II are closer to the curve in the Euler case. This means that the equations in Case II with vanishing numerical viscosity are closer to the Euler equations than the equations in Case I with degenerate diffusion coefficient. Secondly, unlike the alignment in Case I being steady in the stable phase, the alignment in Case II tends to go up in the stable phase, which explains the faster growth of u_1. Thirdly, the strength of the numerical viscosity in Case II does not seem to affect the alignment much, as the curve only changes a little when the resolution is refined. Moreover, they seem to converge to the Euler solution.

3.5. Fitting of the scaling

In this section, we follow the same linear fitting procedure introduced in Section 2.8.1 to study the scaling properties of the solution to the Euler equations with vanishing numerical viscosity. We will see that the solution in Case II has almost the same blowup rates and spatial scales as in Case I, regardless of the strength of the numerical viscosity.

3.5.1. Fitting of growth rates

In Fig. 3.9, we plot the fitting results for the quantity $\|u_1\|_{L^\infty}$ on the time interval $[1.6 \times 10^{-4}, 1.7 \times 10^{-4}]$, which demonstrates excellent linear fitness for both models, $y(t; \|u_1\|_{L^\infty})$ and $\gamma(t; \|u_1\|_{L^\infty})$, with R^2 values very close to 1. It is shown that the fitting of c_{u_1} is close to 1, implying that the growth of u_1 obeys an inverse power law with a power close to 1:

$$\|u_1\|_{L^\infty} \sim (T-t)^{-1}.$$

As we remarked in the previous subsection, the blowup mechanism of Case I is also valid for Case II. In particular, this fitting result matches the asymptotic analysis on the growth rate of u_1 based on the good alignment between u_1 and ψ_1.

We also report in Fig. 3.10 the fitting results for the quantities $\|\omega^z\|_{L^\infty}$, $\|\psi_{1,z}\|_{L^\infty}$, $\||\boldsymbol{u}|^2/2 + p\|_{L^\infty}$, and $\|D^2 p\|_{L^\infty}$. One can see that

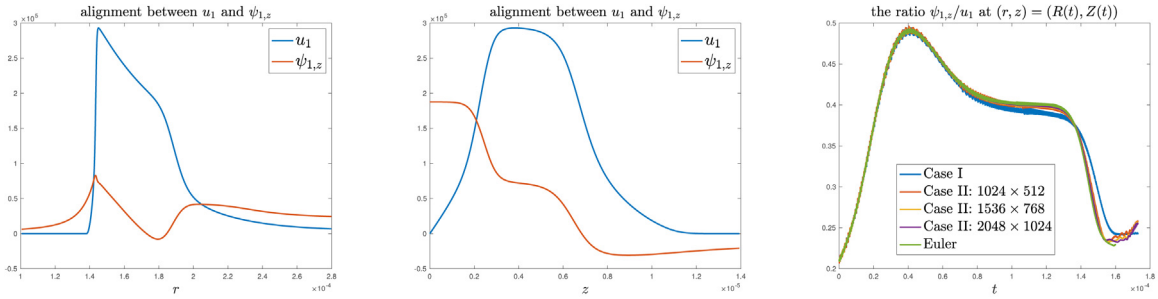

(a) r cross sections of u_1, $\psi_{1,z}$ **(b)** z cross sections of u_1, $\psi_{1,z}$ **(c)** $\psi_{1,z}/u_1$ as a function of time

Fig. 3.8. The alignment between u_1 and $\psi_{1,z}$. (a) and (b): cross sections of u_1 and $\psi_{1,z}$ through the point $(R(t), Z(t))$ at $t = 1.7 \times 10^{-4}$ in Case II. (c): the ratio $\psi_{1,z}/u_1$ at the point $(R(t), Z(t))$ as a function of time in different cases.

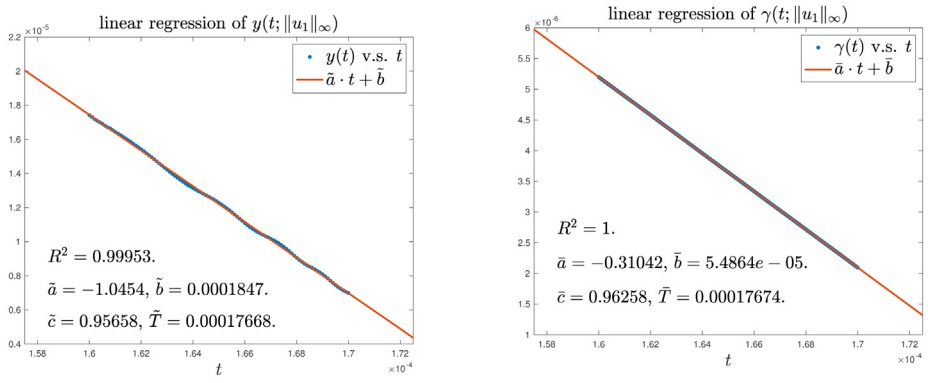

(a) linear regression of $\|u_1(t)\|_{L^\infty}/\|u_1(t)\|'_{L^\infty}$ **(b)** linear regression of $\|u_1(t)\|_{L^\infty}^{1/\bar{c}_{u_1}}$

Fig. 3.9. The linear regression of (a) $y(t;\|u_1\|_{L^\infty})$ and (b) $\gamma(t;\|u_1(t)\|_{L^\infty})$ on the time interval $[t_1, t_2] = [1.6 \times 10^{-4}, 1.7 \times 10^{-4}]$ in Case II. The blue points are the data points obtained from our computation, and the red lines are the linear models. We plot the linear models on a larger interval.

they all have excellent fitness with R^2 values very close to 1, and the growth rates are close to those in Case I:

$$\|\omega^z\|_{L^\infty} \sim (T-t)^{-1.5}, \quad \|\psi_{1,z}\|_{L^\infty} \sim (T-t)^{-1},$$
$$\||\boldsymbol{u}|^2/2 + p\|_{L^\infty} \sim (T-t)^{-1.3}, \quad \|D^2 p\|_{L^\infty} \sim (T-t)^{-2.5}.$$

This suggests a few things. Firstly, the solution in Case II may blow up at a finite time. In particular, the growth rate of ω^z being greater than 1 ($c_{\omega^z} \approx 1.5$) suggests a finite-time singularity by the Beale–Kato–Majda criterion [6], and the growth rate of $D^2 p$ being greater than 2 ($c_{D^2 p} \approx 2.5$) violates the non-blowup criterion proved in [29]. Secondly, the power of $\psi_{1,z}$ being close to 1 (namely the power of u_1) is consistent with our observation of the good alignment between u_1 and $\psi_{1,z}$. Thirdly, the potential two-scale blowup solutions in Case I and Case II are not just qualitatively similar but also have the same blowup scalings. We remark that the fitting of the growth rate of other quantities also gives similar results in both cases. This means that the modification of the diffusion coefficients does not alter the scaling properties of the potential singularity.

In addition, Fig. 3.10(e) reports the linear fitting for the quantity $\|\nabla\boldsymbol{\xi}\|_{L^\infty(\Omega_t)}$ that is described in Section 3.3. The approximate inverse power law $\|\nabla\boldsymbol{\xi}\|_{L^\infty(\Omega_t)} \sim (T-t)^{-1}$ suggests that the integral $\int_0^T \|\nabla\boldsymbol{\xi}\|_{L^\infty(\Omega_t)}\,dt$ shall become infinite at some finite time T, which violates the non-blowup criterion of Constantin–Fefferman–Majda [9]. We remark that the oscillating growth of $\|\nabla\boldsymbol{\xi}\|_{L^\infty(\Omega_t)}$ is probably due to the irregular geometry of the time-dependent set $\Omega_t = \{(r,z) : |\boldsymbol{\omega}(r,z,t)| \geq \frac{1}{2}\|\boldsymbol{\omega}\|_{L^\infty}\}$.

3.5.2. Fitting of spatial scales

We have seen in Section 3.2 that the maximum location $(R(t), Z(t))$ of u_1 also travels towards the origin in Case II, and the ratio $R(t)/Z(t)$ blows up faster. However, our fitting results show that the scalings of $R(t), Z(t)$ are almost the same as those in Case II. In Fig. 3.11, we plot the linear fitting of the γ model (2.11) for $R(t)^{-1}$ and $Z(t)^{-1}$, showing that $R(t)$ and $Z(t)$ satisfy the same power laws in Case I,

$$R(t) \sim (T-t)^{0.5}, \quad Z(t) \sim (T-t),$$

with very good fitness. It is not surprising that $R(t)$ should still behave like $(T-t)^{0.5}$ since its scaling is closely related to the scaling of u_1 through the conservation of total circulation. The total circulation is defined as $\Gamma := ru^\theta = r^2 u_1$, and it is not hard to show that Γ satisfies a maximum principle. We thus have

$$R(t)^2 \cdot \|u_1\|_{L^\infty} = R(t)^2 \cdot u_1(R(t), Z(t)) = \Gamma(R(t), Z(t)) \sim O(1),$$

which implies that $R(t) \sim \|u_1\|_{L^\infty}^{-1/2} \sim (T-t)^{0.5}$. What is more interesting is that $Z(t)$ obeys the same power law as in Case I. It is conjectured in [4] that the power of $Z(t)$ being close to 1 in Case I is because the degenerate diffusion coefficients scale like

$$\nu^r, \nu^z = O(R(t)^2) + O(Z(t)^2) = O(R(t)^2)$$

in the critical blowup region around $(R(t), Z(t))$. The authors also provided an asymptotic scaling analysis to support this conjecture. Here in Case II, the diffusion coefficients are modified so that they are constant in space and scale like $O(R(t)^2)+O(Z(t)^2)$ in time. However, the power of $Z(t)$ remains the same, which seems to support the conjecture that the scaling of $Z(t)$ is chosen by the scaling of the diffusion coefficients near $(R(t), Z(t))$. Then the

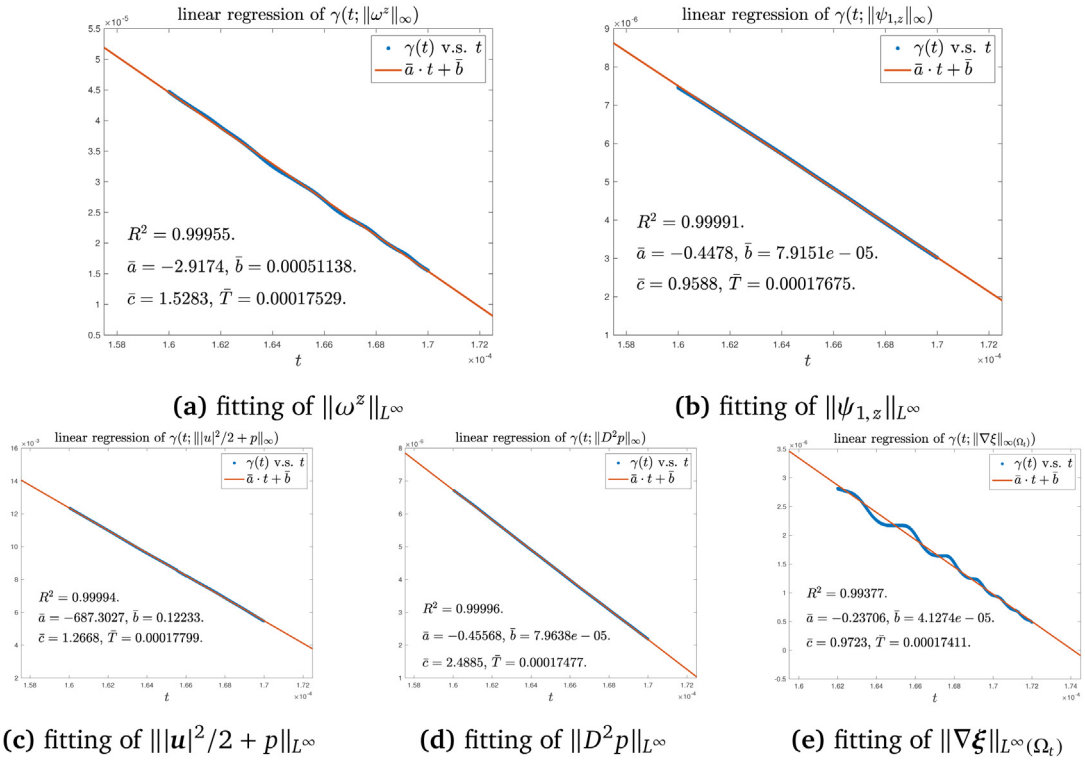

(a) fitting of $\|\omega^z\|_{L^\infty}$ **(b)** fitting of $\|\psi_{1,z}\|_{L^\infty}$

(c) fitting of $\||u|^2/2+p\|_{L^\infty}$ **(d)** fitting of $\|D^2p\|_{L^\infty}$ **(e)** fitting of $\|\nabla\xi\|_{L^\infty(\Omega_t)}$

Fig. 3.10. The linear regression of (a) $\gamma(t;\|\omega^z\|_{L^\infty})$, (b) $\gamma(t;\|\psi_{1,z}\|_{L^\infty})$ (c) $\gamma(t;\||\boldsymbol{u}|^2/2+p\|_{L^\infty})$, (d) $\gamma(t;\|D^2p\|_{L^\infty})$, and (e) $\gamma(t;\|\nabla\boldsymbol{\xi}\|_{L^\infty(\Omega_t)})$. The blue points are the data points obtained from our computation, and the red lines are the linear models. We plot the linear models on a larger interval.

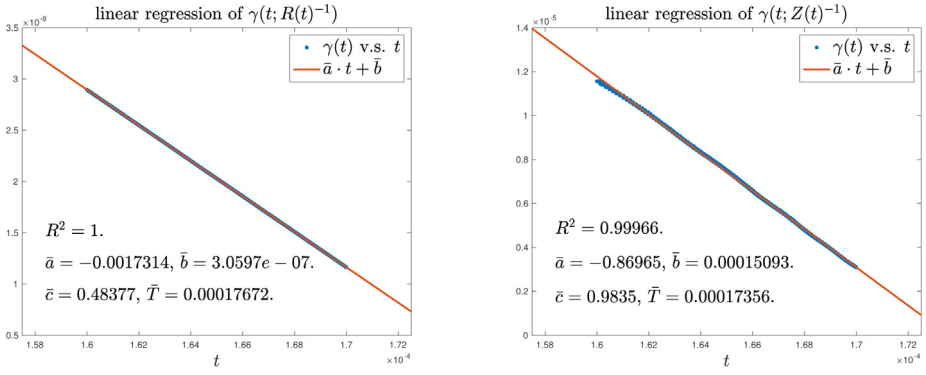

(a) linear regression of $R(t)^{1/\bar{c}_s}$ **(b)** linear regression of $Z(t)^{1/\bar{c}_l}$

Fig. 3.11. The linear regression of (a) $\gamma(t;R(t)^{-1})$ and (b) $\gamma(t;Z(t)^{-1})$ on the time interval $[t_1,t_2]=[1.6\times10^{-4},1.7\times10^{-4}]$. The blue points are the data points obtained from our computation, and the red lines are the linear models. We plot the linear models on a larger interval.

question is whether such scaling can maintain as the strength of the numerical viscosity is reduced by refining the mesh.

3.5.3. Robustness of the fitting

To further study the scaling properties under the change of the diffusion coefficient, we perform linear fitting of the growth rates for the solutions obtained from different resolutions. Recall that the strength of the numerical viscosity decreases as the resolution refines in Case II. Table 3.1 reports the fitting results of different quantities for different resolutions. It appears that the fitting results remain the same up to 2 digits as the numerical viscosity weakens. This is surprising if we believe that it is the scaling of the diffusion coefficients that chooses the spatial scaling of the blowup. On the one hand, the vanishing diffusion coefficients will also be like $O(R(t)^2)+O(Z(t)^2)$, which is consistent with the observed scalings of potential blowup according to the asymptotic analysis in [4]. On the other hand, as the factor h in (3.3) decreases, the solution should converge to the solution to the Euler equations. Does it mean that the Euler solution from the same initial data, if can be continued for a longer time, will also develop a two-scale blowup with the same scalings as in Cases I and II? It would be interesting to explore this question in the future if we can afford enough computational capacity to resolve the Euler solution to a later time.

3.6. Numerical evidence of locally self-similar profiles

As in Case I, the scaling fitting above implies that the solution in Case II may blow up in a self-similar manner. However, the two-scale property only allows self-similar feature to appear

Table 3.1
Linear fitting results of model (2.11) for different quantities computed with different mesh sizes in Case II.

Mesh size	$\|u_1\|_{L^\infty}$		$\|\omega^z\|_{L^\infty}$		$R(t)^{-1}$		$Z(t)^{-1}$	
	$\bar{c}$	R^2	$\bar{c}$	R^2	$\bar{c}$	R^2	$\bar{c}$	R^2
1024 × 512	0.9626	1.00000	1.5283	0.99955	0.4838	1.00000	0.9835	0.99966
1536 × 768	0.9629	1.00000	1.4901	0.99992	0.4826	1.00000	0.9844	0.99987
2048 × 1024	0.9630	1.00000	1.4925	0.99994	0.4825	1.00000	0.9848	0.99989

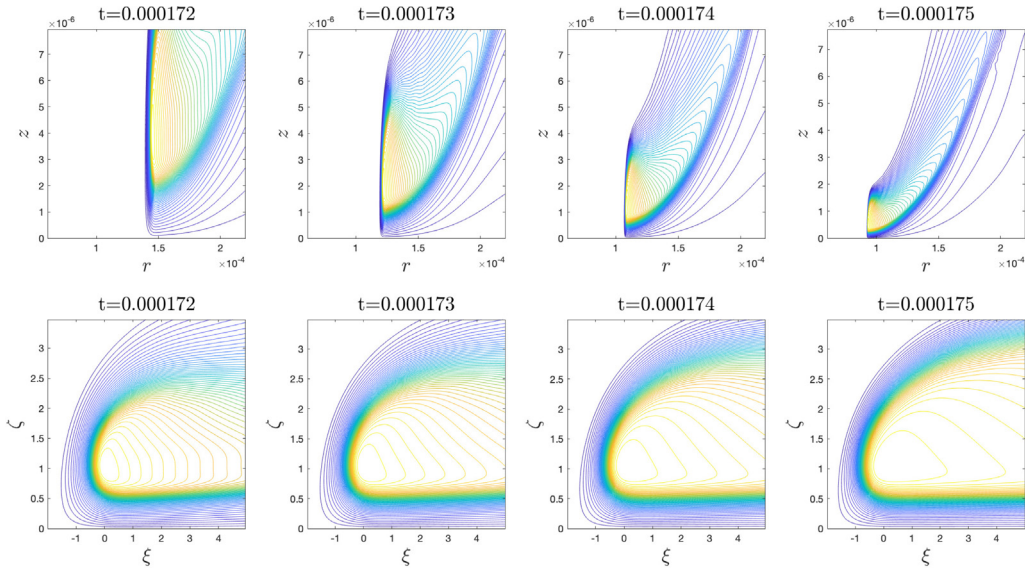

Fig. 3.12. Comparison of the level sets of u_1 at different time instants. First row: original level sets of u_1 in the domain $(r, z) \in [0.6 \times 10^{-4}, 2.2 \times 10^{-4}] \times [0, 8 \times 10^{-6}]$. Second row: rescaled level sets of u_1 as a function of (ξ, ζ) in the domain $(\xi, \zeta) \in [-2, 5] \times [0, 3.5]$.

locally. We thus study the evolution of the rescaled profile in a small-scale neighborhood of $(R(t), Z(t))$.

In Fig. 3.12 and Fig. 3.13, we compare the level sets of u_1 and ω_1, respectively, at different time instants. In the first row of each figure, we plot the solution level sets in a local domain $(r, z) \in [0.6 \times 10^{-4}, 2.2 \times 10^{-4}] \times [0, 8 \times 10^{-6}]$. It is obvious that the profiles of u_1, ω_1 have changed a lot with respect to the physical coordinates from $t = 1.72 \times 10^{-4}$ to $t = 1.75 \times 10^{-4}$. Similar to the changes in Case I, the support of the profiles travels towards the origin with their size shrinking. The sharp front of u_1 and the curved structure of ω_1 also become thinner and thinner.

To investigate the potential local self-similar behavior, we also study the properly rescaled profiles as in Section 2.9. the level sets of the spatially rescaled functions

$$\tilde{u}_1(\xi, \zeta, t) = u_1(Z(t)\xi + R(t), Z(t)\zeta, t),$$
$$\tilde{\omega}_1(\xi, \zeta, t) = \omega_1(Z(t)\xi + R(t), Z(t)\zeta, t).$$

are plotted in the second row of Fig. 3.12 and Fig. 3.13, respectively. As before, the dynamically rescaled coordinates are given by

$$\xi = \frac{r - R(t)}{Z(T)} \sim \frac{r - R(t)}{(T-t)^{c_l}}, \quad \zeta = \frac{z}{Z(T)} \sim \frac{z}{(T-t)^{c_l}}.$$

One can see that the rescaled profiles of u_1, ω_1 seem to converge to a steady structure that barely changes in time. Such converging trend provides strong evidence on the existence of a locally self-similar profile for the solution in Case II.

3.7. Asymptotic scaling analysis

In this subsection, we carry out an asymptotic analysis based on our numerical observations to study the locally self-similar feature of our potential blowup.

Guided by our observations of a two-scale feature in the solution, we propose the following self-similar ansatz with two spatial scalings in the axisymmetric setting:

$$u_1(r, z, t) \sim (T-t)^{-c_u} \bar{U}\left(\frac{r - R(t)}{(T-t)^{c_l}}, \frac{z}{(T-t)^{c_l}}\right), \tag{3.4a}$$

$$\omega_1(r, z, t) \sim (T-t)^{-c_\omega} \bar{\Omega}\left(\frac{r - R(t)}{(T-t)^{c_l}}, \frac{z}{(T-t)^{c_l}}\right), \tag{3.4b}$$

$$\psi_1(r, z, t) \sim (T-t)^{-c_\psi} \bar{\Psi}\left(\frac{r - R(t)}{(T-t)^{c_l}}, \frac{z}{(T-t)^{c_l}}\right), \tag{3.4c}$$

$$R(t) \sim (T-t)^{c_s} R_0. \tag{3.4d}$$

Here $\bar{U}, \bar{\Omega}, \bar{\Psi}$ denote the self-similar profiles of u_1, ω_1, ψ_1 respectively. For notational simplicity, we use c_u, c_ω, c_ψ for $c_{u_1}, c_{\omega_1}, c_{\psi_1}$. As in our previous setting, the reference point $R(t)$ is chosen to be r-coordinate of the maximum location of u_1, and $R_0 > 0$ is some normalization constant. This ansatz depicts that, the solution develops an asymptotically self-similar blowup focusing at the point $(R(t), 0)$ with a local spatial scaling $(T-t)^{c_l}$, and in the mean time, the point $(R(t), 0)$ travels towards the origin with a different length scale $(T-t)^{c_s}$.

A common method to study a self-similar blowup is by substituting the self-similar ansatz (3.4) into the physical Eqs. (2.2) and deriving equations for the potential self-similar profiles $\bar{U}, \bar{\Omega}, \bar{\Psi}$, based on the fundamental assumption that these profiles exist and are smooth functions. A more systematic approach is to introduce time-dependent profile solutions U, Ω, Ψ and treat the potential self-similar profiles $\bar{U}, \bar{\Omega}, \bar{\Psi}$ as the steady state of U, Ω, Ψ. Thus, we can relate (u_1, ω_1, ψ_1) to (U, Ω, Ψ) by a dynamic change of variables given below:

$$u_1(r, z, t) = (T-t)^{-c_u} U(\xi, \zeta, \tau(t)), \tag{3.5a}$$

$$\omega_1(r, z, t) = (T-t)^{-c_\omega} \Omega(\xi, \zeta, \tau(t)), \tag{3.5b}$$

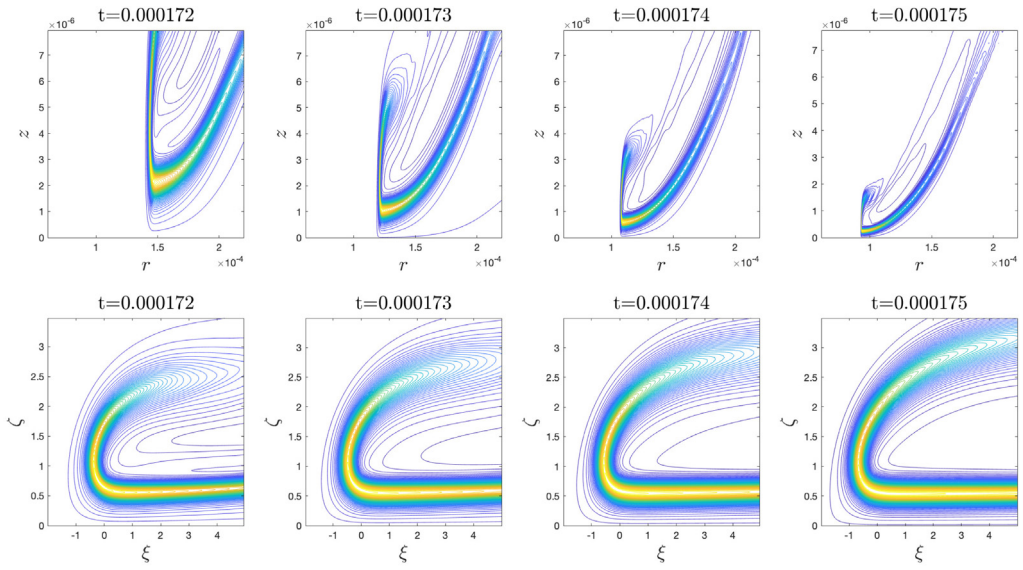

Fig. 3.13. Comparison of the level sets of ω_1 at different time instants. First row: original level sets of u_1 in the domain $(r,z)\in[0.6\times10^{-4},2.2\times10^{-4}]\times[0,8\times10^{-6}]$. Second row: rescaled level sets of ω_1 as a function of (ξ,ζ) in the domain $(\xi,\zeta)\in[-2,5]\times[0,3.5]$.

$$\psi_1(r,z,t)=(T-t)^{-c_\psi}\Psi\left(\xi,\zeta,\tau(t)\right), \tag{3.5c}$$

where

$$\xi:=\frac{r-R(t)}{C_l(t)},\quad \zeta:=\frac{z}{C_l(t)}, \tag{3.5d}$$

and $\tau(t)$ is a rescaled time variable satisfying

$$\tau'(t)=(T-t)^{-1}. \tag{3.5e}$$

Now the self-similar ansatz (3.4) asserts that the profile solutions $U(\xi,\zeta,\tau),\Omega(\xi,\zeta,\tau),\Psi(\xi,\zeta,\tau)$ in the $\xi\zeta$-coordinates should converge to some time-independent profiles $\bar U(\xi,\zeta)$, $\bar\Omega(\xi,\zeta),\bar\Psi(\xi,\zeta)$ as $\tau\to\infty$ (i.e. $t\to T$). In particular, $\bar U,\bar\Omega,\bar\Psi$ should be smooth functions of ξ,ζ.

Before we derive the equations for the profile solutions U,Ω,Ψ, we need to make some assumptions. We first assume that the ansatz (3.4d) is actually an identity:

$$R(t)=(T-s)^{c_s}R_0.$$

Guided by our numerical observations, we make the two-scale assumption:

$$c_s<c_l,\quad \text{or equivalently,}\quad R(t)/C_l(t)\to+\infty\quad\text{as}\quad t\to T. \tag{3.6}$$

Here $C_l:=(T-t)^{c_l}$ is the scale of $Z(t)$. We will also use the following notations

$$C_1(t):=(T-t)^{-1},\quad C_u(t):=(T-t)^{-c_u},\quad C_\omega(t):=(T-t)^{-c_\omega},$$
$$C_\psi(t):=(T-t)^{-c_\psi}.$$

Now we substitute the change of variables (3.5) into the Eqs. (2.2) (with the simplified diffusion terms). For clarity, we do this term by term. For the u_1 Eq. (3.1a), we have

$$\begin{aligned}
u_{1,t}&=C_1C_uU_\tau+c_uC_1C_uU+c_lC_1C_u(\xi U_\xi\\
&\quad+\zeta U_\zeta)+\underline{c_sC_1C_uC_l^{-1}RU_\xi},\\
u^ru_{1,r}+u^zu_{1,z}&=C_\psi C_uC_l^{-1}\left(-\xi\Psi_\zeta U_\xi+(2\Psi+\xi\Psi_\xi)U_\zeta\right)\\
&\quad+\underline{C_\psi C_uC_l^{-2}R\left(-\Psi_\zeta U_\xi+\Psi_\xi U_\zeta\right)},\\
2\psi_{1,z}u_1&=2C_\psi C_uC_l^{-1}\Psi_\zeta U,\\
g_{u_1}&=C_uC_l^{-2}\left(\nu^rU_{\xi\xi}+3\nu^r(\xi+RC_l^{-1})^{-1}U_\xi+\nu^zU_{\zeta\zeta}\right).
\end{aligned} \tag{3.7a}$$

Note that we have used the expressions of u^r,u^z in (3.1d). We have also used the relation (3.5e): $\tau'(t)=(T-t)^{-1}=C_1$. Similarly, for the ω_1 Eq. (3.1b), we have

$$\begin{aligned}
\omega_{1,t}&=C_1C_\omega\Omega_\tau+c_\omega C_1C_\omega\Omega+c_lC_1C_\omega(\xi\Omega_\xi+\zeta\Omega_\zeta)\\
&\quad+\underline{c_sC_1C_\omega C_l^{-1}R\Omega_\xi},\\
u^r\omega_{1,r}+u^z\omega_{1,z}&=C_\psi C_\omega C_l^{-1}\left(-\xi\Psi_\zeta\Omega_\xi+(2\Psi+\xi\Psi_\xi)\Omega_\zeta\right)\\
&\quad+\underline{C_\psi C_\omega C_l^{-2}R\left(-\Psi_\zeta\Omega_\xi+\Psi_\xi\Omega_\zeta\right)},\\
2u_{1,z}u_1&=2C_u^2C_l^{-1}U_\zeta U,\\
g_{\omega_1}&=C_\omega C_l^{-2}\left(\nu^r\Omega_{\xi\xi}+3\nu^r(\xi+RC_l^{-1})^{-1}\Omega_\xi+\nu^z\Omega_{\zeta\zeta}\right).
\end{aligned} \tag{3.7b}$$

Finally, for the Poisson equation (3.1c), we have

$$\begin{aligned}
&-\left(\partial_r^2+\frac{3}{r}\partial_r+\partial_z^2\right)\psi_1=\omega_1\\
&\quad\Longrightarrow\quad -C_\psi C_l^{-2}\left(\partial_\xi^2+\frac{3}{\xi+RC_l^{-1}}\partial_\xi+\partial_\zeta^2\right)\Psi=C_\omega\Omega.
\end{aligned} \tag{3.7c}$$

The next step is to determine the relations between the quantities C_u,C_ω,C_ψ,C_l and R by balancing the terms in each equation of (3.7) in the asymptotic regime $t\to T$, based on the assumption that the limit profiles $\bar U,\bar\Omega,\bar\Psi$ are smooth regular functions of ξ,ζ and are independent of time t. We also assume that the diffusion term are of the same order as the vortex stretching term. This balance is crucial in determining the length scale for C_l or $Z(t)$.

We have underlined some terms in (3.7a) and (3.7b) for some reason to be clarified later. For those terms that are not underlined in (3.7a), the balancing among them as $t\to T$ requires

$$C_1C_u=C_\psi C_uC_l^{-1}\sim\nu C_uC_l^{-2}.$$

Similarly, for those terms that are not underlined in (3.7b), the balance among various terms as $t\to T$ enforces

$$C_1C_\omega=C_\psi C_\omega C_l^{-1}=C_u^2C_l^{-1}\sim\nu C_\omega C_l^{-2}.$$

Finally, for the Poisson equation (3.7c) to balance each other as $t\to T$, we must have

$$C_\psi C_l^{-2}=C_\omega.$$

Summarizing these relations, we obtain that

$$\begin{cases} C_u = C_1, \\ C_\omega = C_1 C_l^{-1}, \\ C_\psi = C_1 C_l, \end{cases} \iff \begin{cases} c_u = 1, \\ c_\omega = 1 + c_l, \\ c_\psi = 1 - c_l, \end{cases} \tag{3.8}$$

and

$$v^r \sim v^z \sim C_1 C_l^2 = (T-t)^{2c_l - 1}. \tag{3.9}$$

Note that the relations (3.8) also imply that the underlined terms can balance with each other in (3.7a) and in (3.7b).

So far, we have already obtained some meaningful information of the blowup rates. If the self-similar ansatz (3.4) is true, then no matter what the spatial scalings c_s, c_l are, the asymptotic blowup rates of u_1, $\psi_{1,z}$ are always 1:

$$\|u_1\|_{L^\infty} \sim C_u = C_1 = (T-t)^{-1},$$
$$\|\psi_{1,z}\|_{L^\infty} \sim C_\psi C_l^{-1} = C_1 = (T-t)^{-1}.$$

This result of the asymptotic analysis is consistent with our discussion in Section 3.4 and fitting results in Section 3.5, which confirms the inverse power law for u_1 and that $\psi_{1,z} \sim u_1$ in the blowup region. To obtain the blowup rate of the other variables, we still need to determine the value of c_l.

To proceed, we need to make use of the conservation of the total circulation, an important physical property of the axisymmetric Euler or Navier–Stokes equations. Recall that the total circulation is defined as

$$\Gamma(r,z,t) := r u^\theta(r,z,t) = r^2 u_1(r,z,t).$$

We remarked in Section 3.5 that Γ satisfies a maximum principle. In fact, it is easy to derive the equation of Γ from the u_1 Eq. (3.1a):

$$\Gamma_t + u^r \Gamma_r + u^z \Gamma_z = v^r \Gamma_{rr} + v^z \Gamma_{zz}, \tag{3.10}$$

which immediately yields the maximum principle. As a result, $\Gamma(R,Z,t) = R^2 u_1(R,Z,t) = O(1)$ as $t \to T$. This means that

$$R(t) \sim \|u_1\|_{L^\infty}^{-1/2} \sim (T-t)^{c_u/2} = (T-t)^{1/2}, \quad \text{or} \quad c_s = \frac{c_u}{2} = \frac{1}{2}.$$

We remark that the relation $c_s = c_u/2 = 1/2$ only relies on the conservation of the maximum circulation and the fact that $c_u = 1$, which are intrinsic to the Eqs. (3.1).

Next, to determine c_l, we need to use the scaling of the vanishing diffusion coefficients,

$$v^r \sim v^z = O(R(t)^2) + O(Z(t)^2).$$

Using $c_s = 1/2$ and the two-scale assumption (3.6) that $c_l > c_s$, we have

$$v^r \sim v^z = O((T-t)^{2c_s}) + O((T-t)^{2c_l}) \sim (T-t)^1.$$

Comparing this with the relation (3.9), we reach that $2c_l - 1 = 1$, or $c_l = 1$.

We have now obtained all the blowup rates and the spatial scalings in the self-similar ansatz (3.4):

$$c_s = 1/2, \quad c_l = 1, \quad c_u = 1, \quad c_\omega = 1 + c_l = 2, \quad c_\psi = 1 - c_l = 0.$$

Moreover, the derivative relations and product relations yield that

$$\omega^z = 2u_1 + r u_{1,r} = O((T-t)^{-c_u}) + O((T-t)^{-c_u + c_s - c_l}) \sim (T-t)^{-1.5}.$$

These results are consistent with the fitting data (Table 3.1) in Section 3.5. For the convenience of comparison, we put together the values of the scaling powers obtained from the numerical fitting (with mesh size 2048 × 1024) and from the asymptotic analysis in Table 3.2. The consistency between the numerical fitting procedures and the asymptotic scaling analysis provides further support for the existence of a finite time locally self-similar blowup of the form (3.4).

Table 3.2
Comparison of the scalings obtained from numerical fitting and from asymptotic analysis.

Scaling powers	c_{u_1}	c_{ω^z}	$c_{\psi_{1,z}}$	c_s	c_l
Numerical fitting	0.9630	1.4925	0.9675	0.4825	0.9848
Asymptotic analysis	1	1.5	1	0.5	1

We have seen that the leading order of the vanishing viscosity coefficients plays a critical role in determining the smaller scale c_l. This was also the case in the related work [4]. As we know, the Euler equations have an extra degree of freedom that formally allows an arbitrarily small scale. It is then wondered whether the order of the viscosity coefficients chooses this particular scaling, or the original Euler equations can automatically develop the same major scalings from the same initial data and boundary conditions.

Recall that we have underlined some terms in (3.7), as they cannot be balanced with the other terms in the analysis. Yet they can balance with each other according to the scaling results. This would mean that the underlined terms should cancel out as $t \to T$ in order for our analysis to hold. Such cancellation will provide extra constraints on the self-similar profiles if they actually exist. A more detailed discussion can be found in [4].

3.8. Further investigation on the viscosity scaling

To gain more insights into the potential relation between the order of the vanishing viscosity coefficients and the smaller spatial scale c_l, we carry out some extra computations with different settings of the numerical viscosity. In particular, we modify the numerical viscosity coefficients in (3.3) by parameterizing their vanishing orders:

$$v_\alpha^r(t) = 256h \cdot \left(\frac{10R(t)^2}{1 + 10^8 R(t)^2} \cdot \left(\frac{R(t)}{R(0)} \right)^\alpha + \frac{10^2 (\sin(\pi Z(t))/\pi)^2}{1 + 10^{11} (\sin(\pi Z(t))/\pi)^2} \cdot \left(\frac{\sin(\pi Z(t))}{\sin(\pi Z(0))} \right)^\alpha \right), \tag{3.11a}$$

$$v_\alpha^z(t) = 256h \cdot \left(\frac{10^{-1} R(t)^2}{1 + 10^8 R(t)^2} \cdot \left(\frac{R(t)}{R(0)} \right)^\alpha + \frac{10^4 (\sin(\pi Z(t))/\pi)^2}{1 + 10^{11} (\sin(\pi Z(t))/\pi)^2} \cdot \left(\frac{\sin(\pi Z(t))}{\sin(\pi Z(0))} \right)^\alpha \right). \tag{3.11b}$$

Such parameterization ensures that (i) $(v_\alpha^r(0), v_\alpha^z(0)) = (v^r(0), v^z(0))$ at $t = 0$ and (ii) $(v_\alpha^r(t), v_\alpha^z(t)) = O(R(t)^{2+\alpha}) + O(Z(t)^{2+\alpha})$ as $(R(t), Z(t))$ converges to the origin. We compare the solutions computed with $\alpha = -1, 0, 1$ to study how the order of viscosity can affect the blowup scaling. Note that the solution with $\alpha = 0$ is the solution in Case II.

We first compare the growth of the solutions with $\alpha = -1$ and $\alpha = 0$ to see whether the stronger vanishing viscosity of order $O(R(t)) + O(Z(t))$ can prevent the potential two-scale blowup in our scenario. Fig. 3.14 compares the growth (in double-log scale) of the solution quantities $\|u_1\|_{L^\infty}$, $\|\boldsymbol{\omega}\|_{L^\infty}$ and $\|D^2 p\|_{L^\infty}$ obtained from both cases. We can see that the solution under the stronger numerical viscosity with $\alpha = -1$ not only grows slower and slower, but even starts to drop after around $t = 1.74 \times 10^{-4}$. This means that the vanishing viscosity of order $O(R(t)) + O(Z(t))$ does not generate another blowup scaling; instead it destroys the scaling of the solution in the previous case. As a reference, it is reported in [4] that, in the same axisymmetric scenario, there is

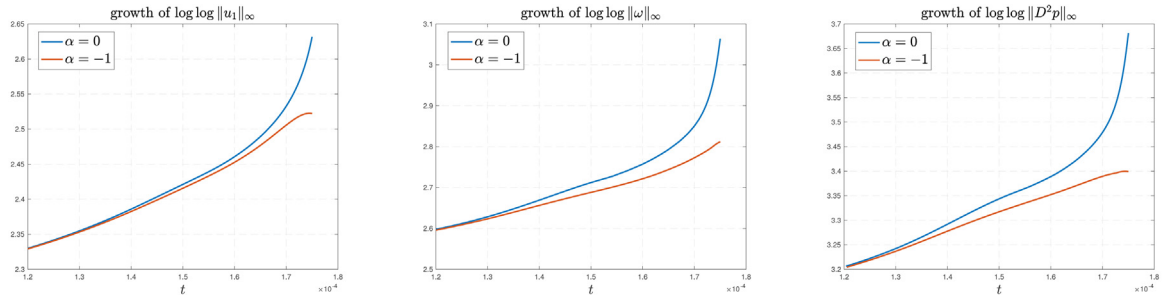

Fig. 3.14. Comparison of the growth of $\log\log\|u_1\|_{L^\infty}$, $\log\log\|\boldsymbol{\omega}\|_{L^\infty}$ and $\log\log\|D^2 p\|_{L^\infty}$ with $\alpha = 0$ and $\alpha = -1$, respectively, in the time window $t \in [1.2 \times 10^{-4}, 1.75 \times 10^{-4}]$.

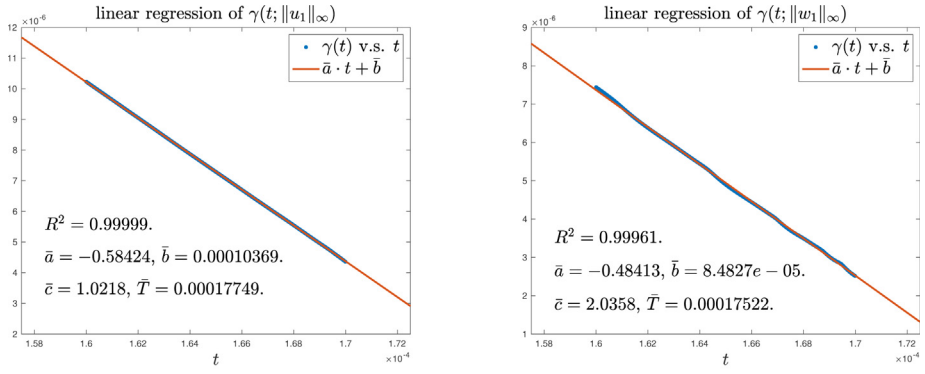

(a) fitting of $\|u_1\|_{L^\infty}$ for $\alpha = 1$

(b) fitting of $\|\omega_1\|_{L^\infty}$ for $\alpha = 1$

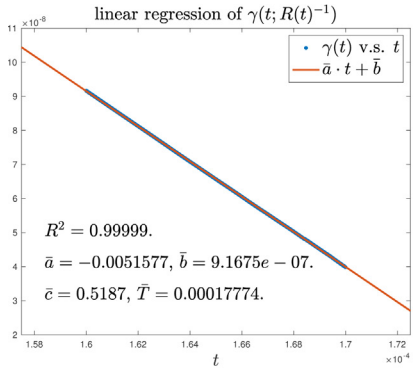

(c) fitting of $R(t)^{-1}$ for $\alpha = 1$

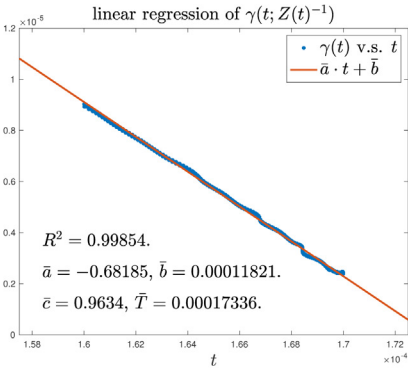

(d) fitting of $Z(t)^{-1}$ for $\alpha = 1$

Fig. 3.15. The linear regression of (a) $\gamma(t; \|u_1\|_{L^\infty})$, (b) $\gamma(t; \|\omega_1\|_{L^\infty})$ (c) $\gamma(t; R(t)^{-1})$, and (d) $\gamma(t; Z(t)^{-1})$ for the solution computed with $\alpha = 1$. The blue points are the data points obtained from our computation, and the red lines are the linear models.

no blowup observed for the original 3D Navier–Stokes equations even with a very small constant viscosity coefficient. Our numerical experiments here further show that the potential two-scale blowup can be suppressed by a time-dependent diffusion effect that does not vanish fast enough.

Next, we study the potential blowup scaling of the solution with $\alpha = 1$ to see whether the smaller scale $c_l = 1$ is intrinsic to the Euler equations. Fig. 3.15 presents the linear regression of the quantities $\|u_1\|_{L^\infty}$, $\|\omega_1\|_{L^\infty}$, $R(t)^{-1}$ and $Z(t)^{-1}$ for the solution with $\alpha = 1$, obtained from the fitting method introduced in Section 2.8.1. Our result shows that these quantities have nice fitting to the approximate power laws

$$\|u_1\|_{L^\infty} \sim (T-t)^{-1}, \quad \|w_1\|_{L^\infty} \sim (T-t)^{-2},$$
$$R(t) \sim (T-t)^{0.5}, \quad Z(t) \sim (T-t),$$

which suggests that the solution has the same blowup scalings as in the case of $\alpha = 0$:

$$c_u = 1, \quad c_\omega = 2, \quad c_s = 1/2, \quad c_l = 1.$$

It is not surprising that $c_u = 2c_s = 1$ for the solution with $\alpha = 1$, since these scalings are irrelevant to the order of the viscosity according to our scaling analysis. What is interesting is that we still have $c_l = 1$ when the vanishing viscosity is of order $O(R(t)^3) + O(Z(t)^3)$. If we honestly go through the same scaling analysis argument with $\nu^r \sim \nu^z = O(R(t)^3) + O(Z(t)^3)$, we should obtain $c_l = 1.25$. Our numerical results, however, suggest that the smaller scale $c_l = 1$ is robust when the vanishing viscosity is weaker than $O(R(t)^2) + O(Z(t)^2)$. We remark that with a weaker numerical viscosity the solution is more sensitive to the Euler instability occurring from the tail region. In fact, we have tried computations with a larger α, but the early emerging of the Euler

instability has prevented us from resolving the solution to a stable phase, just like in the original Euler case.

In summary, our further numerical results imply that the vanishing numerical viscosity of order $O(R(t)^2) + O(Z(t)^2)$ does not select the smaller scale of $c_l = 1$; instead, it is critically compatible with the potential two-scale blowup in our scenario. On the one hand, if the vanishing viscosity is stronger than $O(R(t)^2) + O(Z(t)^2)$, the two-scale blowup will be suppressed. On the other hand, if the vanishing viscosity is weaker than $O(R(t)^2) + O(Z(t)^2)$, the smaller spatial scale $c_l = 1$ still remains, suggesting that it is a characteristic of the underlying solution to the Euler equations. However, to finally determine whether the potential two-scale blowup with the current scalings can happen in the original Euler case, we still need to find a better way to resolve the Euler solution to a later stage. We will continue to pursue this in the future.

4. Concluding remarks

In this paper, we presented strong numerical evidences that the 3D axisymmetric Euler equations with time-dependent vanishing numerical viscosity develop a finite time singularity at the origin. The solution of 3D axisymmetric Euler equations with time-dependent vanishing viscosity shares many common features with those of the solution of 3D axisymmetric Navier–Stokes equations with degenerate diffusion coefficients that we reported in [4]. An important feature of this potential singularity is that the solution develops a two-scale traveling wave solution that travels towards the origin. The hyperbolic flow structure near the center of the traveling wave generates a vacuum region dynamically. The flow evolves into a local "two-phase" flow that separates the "vacuum phase" from the fluid phase by a "moving boundary". We performed careful resolution study and asymptotic scaling analysis to provide further support of the potential locally self-similar blowup.

The rapid decay of the time-dependent viscosity plays a role similar to that of the degenerate diffusion coefficients studied in [4]. It stabilizes the potential singularity formation for the incompressible 3D Euler equations and selects a stable two-scale solution structure. We have also studied the 3D Euler equations using the same initial data in previous works. Without any viscous regularization, the Euler solution quickly developed a very thin structure near the sharp front and the thickness of the sharp front collapses to zero faster than $Z(t)$. Thus, the solution of the 3D Euler equations seems to develop a 3-scale structure, which is extremely difficult to resolve numerically. By applying a first order numerical viscosity with time-dependent vanishing coefficients of order $O(R(t)^2) + O(Z(t)^2)$, we obtained strong numerical evidence that the 3D Euler equations may develop a finite time singularity with scaling properties similar to those of the Navier–Stokes equations with degenerate diffusion coefficients. These scaling properties are found to be robust as the first order numerical viscosity is weakened by refining the resolution.

Declaration of competing interest

The authors declare that they have no known competing financial interests or personal relationships that could have appeared to influence the work reported in this paper.

Acknowledgments

The research was in part supported by NSF, USA Grants DMS-1907977 and DMS-1912654. DH gratefully acknowledges the supports from the Choi Family Postdoc Gift Fund and the Start-up funding from Peking University, China.

References

[1] A. Majda, A. Bertozzi, Vorticity and Incompressible Flow, Vol. 27, Cambridge University Press, 2002.
[2] G. Luo, T.Y. Hou, Potentially singular solutions of the 3D axisymmetric Euler equations, Proc. Natl. Acad. Sci. 111 (36) (2014) 12968–12973.
[3] G. Luo, T.Y. Hou, Toward the finite-time blowup of the 3D axisymmetric Euler equations: a numerical investigation, Multiscale Model. Simul. 12 (4) (2014) 1722–1776.
[4] T.Y. Hou, D. Huang, Potential singularity formation of 3D axisymmetric Navier–Stokes equations with degenerate variable diffusion coefficients, 2021, ArXiv:2102.06663.
[5] T.Y. Hou, C. Li, Dynamic stability of the three-dimensional axisymmetric Navier–Stokes equations with swirl, CPAM 61 (5) (2008) 661–697.
[6] J. Beale, T. Kato, A. Majda, Remarks on the breakdown of smooth solutions for the 3-D Euler equations, Comm. Math. Phys. 94 (1) (1984) 61–66.
[7] T.Y. Hou, The nearly singular behavior of the 3D Navier–Stokes equations, 2021, ArXiv:2107.06509 [Physics.Flu-Dyn].
[8] T.Y. Hou, Potential singularity of the 3D Euler equations in the interior domain, 2021, ArXiv:2107.05870 [Math.AP].
[9] P. Constantin, C. Fefferman, A. Majda, Geometric constraints on potentially singular solutions for the 3-D Euler equations, Comm. Partial Differential Equations 21 (1996) 559–571.
[10] J. Deng, T.Y. Hou, X. Yu, Geometric properties and non-blowup of 3D incompressible Euler flow, Comm. Partial Differential Equations 30 (2005) 225–243.
[11] T.M. Elgindi, Finite-time singularity formation for $C^{1,\alpha}$ solutions to the incompressible Euler equations on $\mathbb{R}^3$, Ann. of Math. 194 (3) (2021) 647–727.
[12] T.M. Elgindi, T. Ghoul, N. Masmoudi, On the stability of self-similar blowup for $C^{1,\alpha}$ solutions to the incompressible Euler equations on R^3, 2019, ArXiv:1910.14071.
[13] A. Kiselev, V. Sverak, Small scale creation for solutions of the incompressible two dimensional Euler equation, Ann. of Math. 180 (2014) 1205–1220.
[14] K. Choi, T.Y. Hou, A. Kiselev, G. Luo, V. Sverak, Y. Yao, On the finite-time blowup of a 1D model for the 3D axisymmetric Euler equations, CPAM 70 (11) (2017) 2218–2243.
[15] A. Kiselev, L. Ryzhik, Y. Yao, A. Zlatos, Finite time singularity for the modified SQG patch equation, Ann. of Math. 184 (2016) 909–948.
[16] J. Chen, T.Y. Hou, Finite time blowup of 2D Boussinesq and 3d Euler equations with $C^{1,\alpha}$ velocity and boundary, CMP 383 (3) (2021) 1559–1667.
[17] J. Chen, T.Y. Hou, D. Huang, On the finite time blowup of the De Gregorio model for the 3D Euler equations, CPAM 74 (6) (2021) 1282–1350.
[18] A. Kiselev, Small scales and singularity formation in fluid dynamics, in: Proceedings of the International Congress of Mathematicians, Vol.3, 2018.
[19] R. Grauer, T.C. Sideris, Numerical computation of 3D incompressible ideal fluids with swirl, Phys. Rev. Lett. 67 (1991) 3511–3514.
[20] A. Pumir, E.D. Siggia, Development of singular solutions to the axisymmetric Euler equations, Phys. Fluids A 4 (1992) 1472–1491.
[21] W. E, C.-W. Shu, Small-scale structures in Boussinesq convection, Phys. Fluids 6 (1994) 49–58.
[22] O.N. Boratav, R.B. Pelz, Direct numerical simulation of transition to turbulence from a high-symmetry initial condition, Phys. Fluids 6 (1994) 2757–2784.
[23] R.M. Kerr, Evidence for a singularity of the three-dimensional incompressible Euler equations, Phys. Fluids A 5 (1993) 1725–1746.
[24] T.Y. Hou, R. Li, Dynamic depletion of vortex stretching and non-blowup of the 3-D incompressible Euler equations, J. Nonlinear Sci. 16 (2006) 639–664.
[25] T.Y. Hou, R. Li, Blowup or no blowup? The interplay between theory and numerics, Physica D. 237 (2008) 1937–1944.
[26] M. Brenner, S. Hormoz, A. Pumir, Potential singularity mechanism for the Euler equations, Phys. Rev. Fluids 1 (2016) 084503.
[27] J. Gibbon, The three-dimensional Euler equations: Where do we stand? Physica D 237 (2008) 1894–1904.
[28] G. Seregin, V. Sverak, Navier–Stokes equations with lower bounds on the pressure, Arch. Ration. Mech. Anal. 9 (1) (2002) 65–86.
[29] D. Chae, P. Constantin, On a type I singularity condition in terms of the pressure for the Euler equations in $\mathbb{R}^3$, 2020, arXiv preprint arXiv:2012.11948.